

Fall 2013

Effect of temperature on tunneling and quantum efficiency in cigs solar cells

Sizhan Liu

New Jersey Institute of Technology

Follow this and additional works at: <https://digitalcommons.njit.edu/theses>



Part of the [Materials Science and Engineering Commons](#)

Recommended Citation

Liu, Sizhan, "Effect of temperature on tunneling and quantum efficiency in cigs solar cells" (2013). *Theses*. 187.
<https://digitalcommons.njit.edu/theses/187>

This Thesis is brought to you for free and open access by the Theses and Dissertations at Digital Commons @ NJIT. It has been accepted for inclusion in Theses by an authorized administrator of Digital Commons @ NJIT. For more information, please contact digitalcommons@njit.edu.

Copyright Warning & Restrictions

The copyright law of the United States (Title 17, United States Code) governs the making of photocopies or other reproductions of copyrighted material.

Under certain conditions specified in the law, libraries and archives are authorized to furnish a photocopy or other reproduction. One of these specified conditions is that the photocopy or reproduction is not to be “used for any purpose other than private study, scholarship, or research.” If a user makes a request for, or later uses, a photocopy or reproduction for purposes in excess of “fair use” that user may be liable for copyright infringement,

This institution reserves the right to refuse to accept a copying order if, in its judgment, fulfillment of the order would involve violation of copyright law.

Please Note: The author retains the copyright while the New Jersey Institute of Technology reserves the right to distribute this thesis or dissertation

Printing note: If you do not wish to print this page, then select “Pages from: first page # to: last page #” on the print dialog screen

The Van Houten library has removed some of the personal information and all signatures from the approval page and biographical sketches of theses and dissertations in order to protect the identity of NJIT graduates and faculty.

ABSTRACT

EFFECT OF TEMPERATURE ON TUNNELING AND QUANTUM EFFICIENCY IN CIGS SOLAR CELLS

Sizhan Liu

Utilizing the two-band approximation and Wentzel-Kramers-Brillouin (WKB) approximation, by including the temperature-dependent effective masses and nonparabolicity effects, an investigation of the temperature dependent band-to-band tunneling process is discussed. In comparison with the parabolic approximation and non-parabolic approximation, the tunneling probability is strongly dependent on the non-parabolicity factor. The temperature dependence of the energy band gap, electron effective mass and light hole effective mass is investigated. The tunneling current density function is derived by a series representation of the incomplete gamma function with non-parabolic effect and its variation at low temperature is also investigated. When the Fermi level of holes is in excess of that of electrons, i.e., $E_{Fp} \gg E_{Fn}$, the current density function can be successfully simplified as the Fowler-Nordheim formulation. The quantum efficiency model, for CIGS solar cells, is discussed. Device modeling and simulation studies of a $\text{Cu}(\text{In}_{1-x}\text{Ga}_x)\text{Se}_2$ (CIGS) thin film solar cell are carried out. A variety of graded band-gap structures, including space charge region (SCR) grading, back surface region grading, and double grading of the CIGS absorber layer are considered. A position-dependent absorption coefficient $\alpha(x, h\nu)$ is obtained by a differential equation for the photon flux $\varphi(x, h\nu)$. The quantum efficiency can be calculated by $\text{IQE} = (\varphi_1 - \varphi_2) / \varphi_3$. The temperature dependence of the quantum efficiency is also investigated in this thesis.

**EFFECT OF TEMPERATURE ON TUNNELING AND QUANTUM
EFFICIENCY IN CIGS SOLAR CELLS**

**by
Sizhan Liu**

**A Thesis
Submitted to the Faculty of
New Jersey Institute of Technology
in Partial Fulfillment of the Requirements for the Degree of
Master of Science in Materials Science and Engineering
Interdisciplinary Program in Materials Science and Engineering**

January 2014

Copyright © 2014 by Sizhan Liu

ALL RIGHTS RESERVED

APPROVAL PAGE

**EFFECT OF TEMPERATURE ON TUNNELING AND QUANTUM
EFFICIENCY IN CIGS SOLAR CELLS**

Sizhan Liu

Dr. Nuggehalli M. Ravindra, Thesis Advisor
Professor of Physics, NJIT

Date

Dr. Halina Opyrchal, Committee Member
Senior University Lecturer of Physics, NJIT

Date

Dr. Tao Zhou, Committee Member
Associate Professor of Physics, NJIT

Date

Dr. Ken Ahn, Committee Member
Associate Professor of Physics, NJIT

Date

BIOGRAPHICAL SKETCH

Author: Sizhan Liu
Degree: Master of Science
Date: January 2014

Undergraduate and Graduate Education:

- Master of Science in Materials Science and Engineering, New Jersey Institute of Technology, Newark, NJ, 2014
- Bachelor of Science in Materials Science and Engineering, Tongji University, Shanghai, P. R. China, 2012

Major: Materials Science and Engineering

Presentations and Publications:

Sizhan Liu and Huang Zhuping, "Research on creep rupture of domestic HR3C heat resistant steel," *Metallic Function Materials* 20.1 (2013): 19-22.

< To my family, friends and teachers >

ACKNOWLEDGMENTS

The end of my graduate studies is a good time to stop and give thanks to all those who helped me to get to this milestone. As I complete my Master's degree, the end of over twenty years of schooling leaves me with some trepidation, but also excitement at the possibilities that await me. Without those who have guided me along the way, the arc of my life, and correspondingly this dissertation, would have been far different.

First and foremost, I would like to thank my parents for all they have done for me. Their unending expression of love and pride in my choices allowed me to take risks in my educational path while knowing that, irrespective of what happened, I had their support.

Next, I cannot adequately express in words of my thanks to Prof. N. M. Ravindra, my advisor. To me, a professor is a mentor, a teacher, and a scholar all in one. Prof. Ravi exemplifies the best in each of these roles. I really appreciate his help when I most needed it, he stood by me. I will always appreciate that. I also give my sincere thanks to my thesis committee members, Dr. Halina Opyrchal, Dr. Tao Zhou and Dr. Ken Ahn.

Finally, I thank everyone who I interacted with at NJIT. I learned so much from the people that made this work possible.

TABLE OF CONTENTS

Chapter	Page
1 INTRODUCTION	1
2 TEMPERATURE DEPENDENCE OF BAND GAP	3
2.1 Varshni Relation	3
2.2 Bose-Einstein Model	4
2.3 Temperature-dependent Energy Gap of GaAs	7
3 EFFECTIVE MASS	8
3.1 Non-parabolic Effect On Effective Mass	8
3.2 Empirical Models	11
4 TUNNELING	15
4.1 Introduction	15
4.2 Tunneling Mechanisms	17
4.3 Band-to-band Tunneling in Diodes	18
4.4 Complex Band Structure	20
4.4.1 Parabolic Approximation	20
4.4.2 Non-parabolic Approximation	21
4.5 Tunneling Probability	25
4.5.1 Transmission Coefficient Modeling	25
4.5.2 The Wentzel-Kramers-Brillouin Approximation	27
4.5.3 Temperature-dependent Transmission Coefficient	31
4.6 Tunneling Current Density	32

TABLE OF CONTENTS
(Continued)

Chapter	Page
4.6.1 The Density of States	32
4.6.2 The Tsu-Esaki Model	33
4.6.3 Supply Function Modeling	39
4.6.4 Fermi-Dirac Distribution	40
4.6.5 Tunneling Current Density Function	41
4.6.6 Temperature-dependent Tunneling Current Density	49
5 QUANTUM EFFICIENCY MODEL- APPLICATION TO SOLAR CELLS	51
5.1 Introduction	51
5.2 Photon Energy and Flux	53
5.3 Generation Rate	55
5.4 Absorption Coefficient	56
5.4.1 Absorption Coefficient with Urbach Tail	56
5.4.2 Urbach Energy	57
5.5 Quantum Efficiency	61
5.6 Quantum Efficiency Model	61
5.6.1 The Position-dependent Absorption Coefficient	62
5.6.2 Modeling of Double-graded Band Gap	63
5.6.3 Quantum Efficiency Calculations	64
5.6.4 Temperature-dependent Quantum Efficiency	70
6 CONCLUSIONS	72

TABLE OF CONTENTS
(Continued)

Chapter	Page
APPENDIX FERMI-DIRAC INTEGRALS	74
REFERENCES	76

LIST OF TABLES

Table	Page
2.1 Varshni Equation Constants for GaAs, Si, and Ge	3
2.2 Parameters for the Temperature Dependence of the Band Gap According to Eq. (1.3) and Eq. (1.4) for Various Semiconductors.....	6
2.3 List of Various Fitting Parameters in Different Models	7
5.1 CIGS Solar Cells with Various Absorber Band Gap Profiles	53

LIST OF FIGURES

Figure	Page
2.1 Temperature dependence of energy gap of GaAs, Si and Ge	4
2.2 Temperature dependent energy band gap of GaAs, with different models, ranging from 0K to 500K	7
3.1 Temperature dependence of the effective masses, in GaAs, ranging from 0K to 500K according to Hrivnak's model	14
4.1 Schematic of MOSFET structure	15
4.2 Schematic of the tunneling processes in a silicon-dielectric-silicon structure	18
4.3 Band diagram for the tunneling electron with nonzero perpendicular momentum in the valance band and conduction band	19
4.4 Energy vs imaginary wave vector within the band gap according to Eq. (1) and Eq. (2) and the tunneling path assumed in my calculation (solid line) with various values of β . ($\square \beta=2$, $\circ \beta=3$, $\Delta \beta=4$, $+ \beta \rightarrow \infty$)	23
4.5 Complex band structure for various electron-hole effective mass ratio $\gamma=m^*/m^*_c$. ($\square \gamma=1$, $\Delta \gamma=1.25$, $\circ \gamma=1.5$, $+ \gamma=1.75$, $\diamond \gamma=2$)	24
4.6 Schematic of an energy barrier of a single-layer dielectric	26
4.7 $E-k$ plot depicting the increased band gap incurred by perpendicular momentum.	27
4.8 The value of prefactor δ according to Eq. (3.11) for the variation of β	30
4.9 Temperature-dependent transmission coefficient of NPA with various values of β . ($\square \beta=2$, $\circ \beta=3$, $\Delta \beta=4$, $+ \beta \rightarrow \infty$)	32
4.10 The current density J of parabolic band structure and non-parabolic band structure versus \mathcal{A}	47
4.11 The current density J with various β	48
4.12 Temperature dependent tunneling current density is calculated according to Eq. (3.13) with Eq. (3.16)	50

LIST OF FIGURES
(Continued)

Figure	Page
5.1 Schematic cross section of a typical Cu(InGa)Se ₂ solar cell	51
5.2 Absorption coefficient of a semiconductor with band gap E_g versus energy	57
5.3 Urbach tail occurrence scheme	57
5.4 Energy diagram of a double-graded band gap absorber	63
5.5 Internal quantum efficiency IQE vs. wavelength for increasing β (blue $\beta=0.2$, purple $\beta=0.5$, red $\beta=0.8$), assuming $A=5 \times 10^4 \text{ cm}^{-1} \text{ eV}^{-1/2}$, $E_{back}=1.54 \text{ eV}$, $E_{min}=1.04 \text{ eV}$, $E_{front}=1.34 \text{ eV}$, $\gamma=0.2$, $E_U=0.05$	68
5.6 The comparison of simulation results and experimental results	69
5.7 The quantum efficiency of the CIGS solar cell absorber as a function of temperature and wavelength. The wavelength was varied from 0.2 μm to 1.1 μm , and temperature from 0K to 600K	70

CHAPTER 1

INTRODUCTION

This chapter introduces and provides an overview of the research that is to be undertaken in this study.

Chapter 2 is a comprehensive literature review of various models on temperature dependence of the band gap, such as the Varshni relation and Bose-Einstein model. The temperature-dependent energy band gap of GaAs, with different models, ranging from 0K to 500K is investigated. The temperature dependence of the band gap is used to calculate the variation in tunneling probability with temperature.

In Chapter 3, the effective mass is derived from Kane's two-band model that considers both the $k \cdot p$ interaction and spin-orbit coupling as perturbations to the classical Hamiltonian in isotropic materials. The effective mass is achieved by non-parabolic dispersion relation of Kane's model. The dispersion relation implies that, at the bottom of the band, a parabolic relation $E = \hbar^2 k^2 / 2m_e^2$ is preserved, while a small, non-parabolic correction αE^2 is observed for higher E. It is to be noted that the non-parabolicity factor, α , depends on the electron effective mass as well as the band gap. The empirical models of effective mass, with non-parabolic effect, are also described. The light hole effective mass and the electron effective mass are used to estimate the temperature dependence of the tunneling probability and the tunneling current density with non-parabolic effects.

In Chapter 4, quantum-mechanical tunneling is investigated especially in the non-parabolic band structure and with a variation of temperature. The conventional non-parabolic approximation of real band structures can be modified and generalized to approximate the complex band structures of common semiconductors with a significant

improvement in accuracy in comparison with the parabolic approximation. The tunneling current density is calculated from a non-parabolic dispersion relation. In the calculation, the supply function is replaced by a step function and a series representation of the incomplete gamma function is used to reduce the solution. The tunneling current density is greatly influenced by the behavior of the band structure so that the non-parabolic behavior of the band structure has additional contribution to the current density. The growth rate of the tunneling current density which has contributions from non-parabolic band behavior and parabolic band behavior, with increase of temperature, is almost the same.

The quantum efficiency model, based on CIGS solar cells, is discussed in Chapter 5. Device modeling and simulation studies of $\text{Cu}(\text{In}_{1-x}\text{Ga}_x)\text{Se}_2$ (CIGS) thin film solar cells have been carried out. There are a variety of graded band-gap structures, including space charge region (SCR) grading, back surface region grading, and double grading of the CIGS absorber layer. A grading in the absorber can improve cell performance and some modern CIGS solar cells already have such a graded band gap profile. It is difficult to discern the real benefit of grading, as varying material properties through the cell implies changing the mean value of the studied parameter, and it is almost impossible to produce a reference cell having the same properties as the studied cell. Hence, if one wants to study grading properties thoroughly, one should use numerical simulations. A position-dependent absorption coefficient $\alpha(x, h\nu)$ is obtained by a differential equation for the photon flux $\varphi(x, h\nu)$. The quantum efficiency can thus be calculated by $\text{IQE}=(\varphi_1-\varphi_2)/\varphi_3$. The temperature dependence of the quantum efficiency is also described in this thesis.

CHAPTER 2

TEMPERATURE DEPENDENCE OF BAND GAP

2.1 Varshni Relation

The effect of temperature on band gap energy shrinkage has been quantified through several empirical or semi-empirical relations. The energy gap behavior, as a function of temperature, is reported in Figure 2.1. Among the empirical relations, the Varshni relation [1] is often used to assess the nonlinear temperature dependent band gap shift:

$$E_g = E_g(0) - \frac{\alpha T^2}{T + \beta} \quad (2.1)$$

where, α and β are fitting parameters characteristic of a given material. $E_g(0)$ is the band gap of the semiconductor at 0K. The Varshni relation is a combination of quadratic low temperature asymptotic behavior with linear high temperature dependence [2, 3]. The Varshni relation fits well for low temperatures (up to 360K); however, it shows deviation from experimental values, above 360K [4].

Table 2.1 Varshni Equation Constants for GaAs, Si, and Ge [5]

Material	$E_g(0)$ (eV)	α (eVK ⁻¹)	β (eVK ⁻¹)
GaAs	1.519	5.405×10^{-4}	204
Si	1.17	4.73×10^{-4}	636
Ge	0.7437	4.77×10^{-4}	235

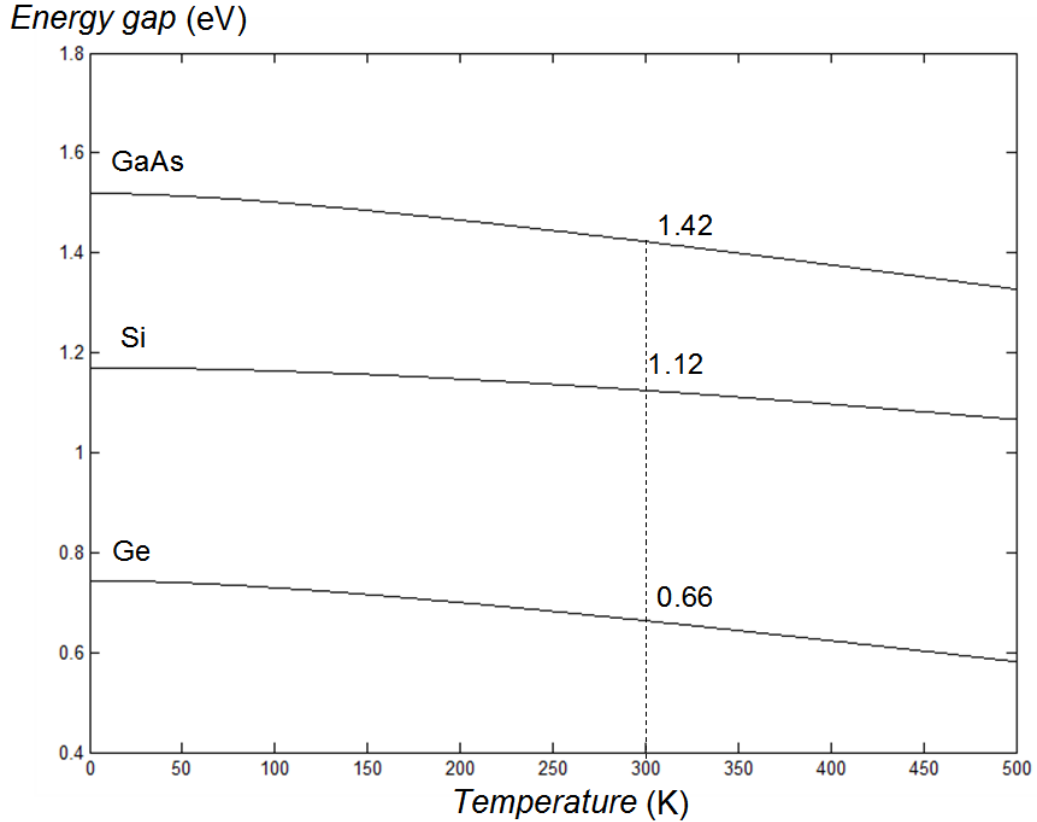


Figure 2.1 Temperature dependence of energy gap of GaAs, Si and Ge.

Table 2.1 and Eq. (2.1) are used to generate Figure 2.1, which shows that the band gaps of the three materials decrease as temperature increases. The labeled points are the band gap of each material at room temperature. Generally, the energy gap of semiconductors decreases with increase in temperature. However, there are some exceptions such as the lead chalcogenides – PbS, PbSe and PbTe in which the energy gap increases with increase in temperature [84].

2.2 Bose-Einstein Model

The Bose-Einstein model, which considers electron interaction within crystals, also relates energy shift and temperature with Debye energy. According to this model, the band gap energy can be determined from [6]:

$$E_g(T) = E_g(0) - \frac{2\alpha_B}{\exp(\Theta_E/T) - 1} \quad (2.2)$$

where, α_B is a parameter associated with the strength of the exciton-phonon interaction within the crystal; the Einstein characteristic temperature, Θ_E , is the average temperature of phonons interacting with the electronic subsystem. The Debye temperature for an Einstein oscillator can be determined from the relationship: $\Theta_D = 4/3\Theta_E$.

A more precise and physically motivated formula which is a direct replacement of the Varshni equation with phonon interaction, based on a Bose-Einstein phonon model, has been given in [7]:

$$E_g(T) = E_g(0) - 2\alpha_B\Theta_B \left[\coth\left(\frac{\Theta_B}{2kT}\right) - 1 \right] \quad (2.3)$$

where, $E_g(0)$ is the band gap at zero temperature, α_B is a dimensionless coupling constant, and $k\Theta_B$ is an average phonon energy. Typical values of these parameters are presented in Table 2.2. This model proposes a better description of the fairly flat dependence of energy gap at low temperatures. However, experimentally, the dependence of the energy gap at low temperatures is rather quadratic.

A more elaborate model takes into account a more variable phonon dispersion, including optical phonons, and proposes the four-parameter formula:

$$E_g(T) = E_g(0) - \alpha' \Theta \left[\frac{1 - 3\Delta^2}{\exp(2/\gamma)} + \frac{3\Delta^2}{2} (\sqrt[6]{1 + \beta} - 1) \right] \quad (2.4)$$

$$\beta = \frac{\pi^2}{3(1 + \Delta^2)} \gamma^2 + \frac{3\Delta^2 - 1}{4} \gamma^3 + \frac{8}{3} \gamma^4 + \gamma^6 \quad (2.5)$$

$$\gamma = 2T / \Theta \quad (2.6)$$

where, α' is the high-temperature limiting magnitude of the slope of the order of several 10^{-4} eV/K, Θ is an effective average phonon temperature and Δ is related to the phonon dispersion.

Table 2.2 Parameters for the Temperature Dependence of the Band Gap According to Eq. (2.3) and Eq. (2.4) for Various Semiconductors [8]

	$\alpha'(10^{-4}$ eV/K)	Θ (K)	Δ	$\alpha_B(10^{-4}$ eV/K)	Θ_B (K)
Si	3.23	446	0.51	2.82	351
Ge	4.13	253	0.49		
GaAs	4.77	252	0.43	5.12	313
InP	3.96	274	0.48		
InAs	2.82	147	0.68		
ZnSe	5.00	218	0.36		
ZnO	3.8	659	0.54		

2.3 Temperature-dependent Energy Gap of GaAs

Table 2.3 List of Various Fitting Parameters in Different Models

Model or equation	Fitting parameter	Fitting parameter	Fitting parameter
Eq. (1.1)	$\alpha=5.41\times 10^{-4} \text{ eVK}^{-1}$	$\beta=204\text{K}$	
Eq. (1.3)	$\alpha_B=5.12\times 10^{-4} \text{ eVK}^{-1}$	$\Theta_B=313\text{K}$	
Eq. (1.4)	$\alpha'=4.77$	$\Theta=252\text{eV}$	$\Delta=0.43$

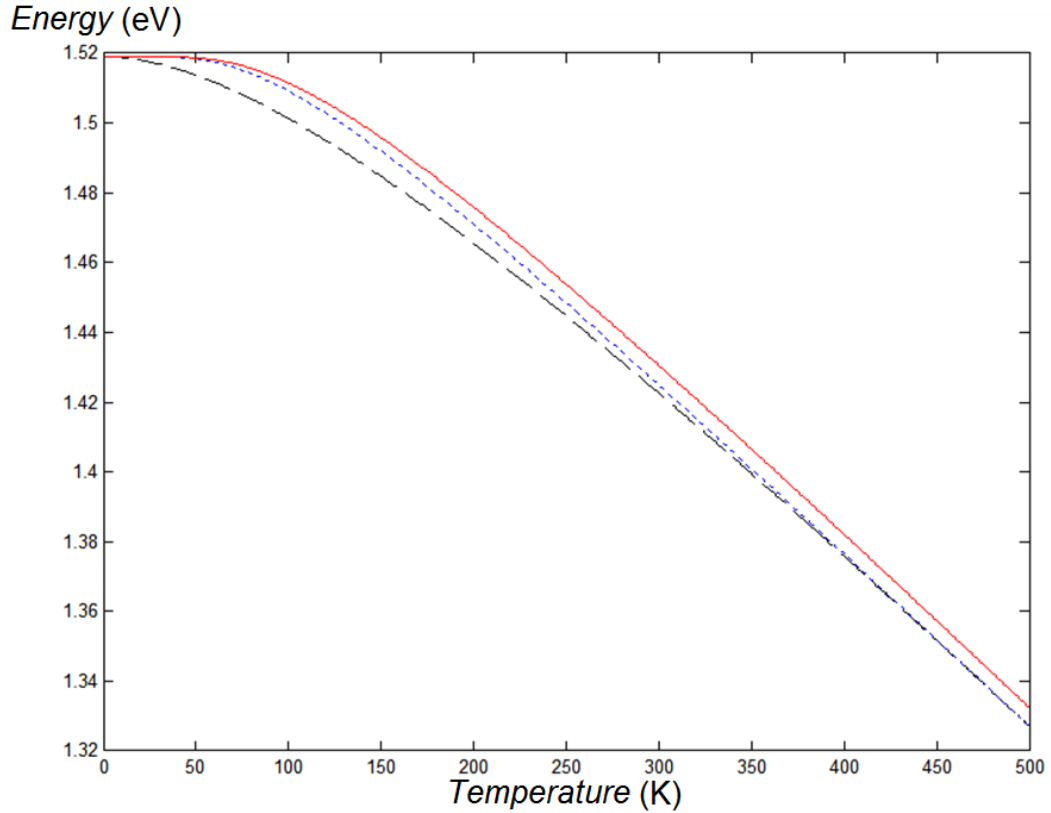


Figure 2.2 Temperature dependent energy band gap of GaAs, with different models, ranging from 0K to 500K. Dashed line is from Varishni's model according to Eq. (2.1), the dotted line is according to Eq. (2.3) and the solid line is according to Eq. (2.4). The parameters used in the calculations are shown in Table 2.3.

CHAPTER 3
EFFECTIVE MASS

3.1 Non-parabolic Effect on Effective Mass

Kane considered both the $\mathbf{k}\cdot\mathbf{p}$ interaction and the spin-orbit coupling as perturbations to the classical Hamiltonian in isotropic materials. The resulting Hamiltonian can be diagonalized exactly and does not require the carrier kinetic energy E to be small. However, Kane's solution is accurate only if the interaction with other bands can be neglected which does imply a small E . If E_g is defined as the prime band gap and Δ as the split-off splitting, the solution can be written as [9]:

$$E'(E' + E_g)(E' + E_g + \Delta) = k^2 P^2 \left(E' + E_g + \frac{2}{3} \Delta \right) \quad (3.1)$$

where, $E' = E - (\hbar^2 k^2 / 2m_0^2)$ and P^2 is the square of Kane's matrix element of the linear momentum between conduction band and valence band at $k = 0$. For the cases under consideration, $\hbar^2 k^2 / 2m_0^2$ is much smaller than $E(k)$, $E' \approx E(k)$, $E' \ll E_g$, and $\Delta \ll E_g$, the dispersion relation is $\hbar^2 k^2 / 2m_0^2 = E(1 + E/E_g)$. However, the approximations, $E' \ll E_g$, and $\Delta \ll E_g$, are not valid in general such as in the case of InAs. Since we are looking for a solution near the band extremum, i.e., $E \approx 0$, Eq. (3.1) can be approximated by preserving only E^2 terms to find the dispersion relation in non-parabolic condition:

$$\frac{\hbar^2 k^2}{2m_{e0}} \cong E + \alpha E^2 \quad (3.2)$$

where, m_e is the electron effective mass at the band minimum and α is the non-parabolicity factor. Using the comprehensive $\mathbf{k}\cdot\mathbf{p}$ perturbation approach, the electron effective mass at the bottom of the conduction band can be expressed in a following form [10, 11]:

$$\frac{1}{m_e} = \frac{1}{m_0} + \frac{2P^2}{\hbar^2 E_g} \frac{E_g + 2\Delta/3}{E_g + \Delta} \quad (3.3)$$

The first term describes the undisturbed effective mass whereas the second term represents the non-parabolic correction [10]. If the spin-orbit splitting and the momentum matrix elements are assumed to be constant and independent of temperature, the temperature independence of the effective mass is just a direct consequence of the temperature dependence of the energy band gap. It is given by:

$$\alpha = \frac{1}{E_g} \left(1 - \frac{m_e}{m_0} \right)^2 \quad (3.4)$$

The dispersion relation implies that, at the bottom of the band, a parabolic relation $E = \hbar^2 k^2 / 2m_e^2$ is preserved, while a small, non-parabolic correction αE^2 is observed for higher E . Note that the non-parabolicity factor, α , depends on the electron effective mass as well as the band gap. The effective mass is generally energy dependent and can be calculated for non-parabolic materials from Eq. (3.2) as:

$$m^*(E) = \hbar^2 k \left(\frac{dE}{dk} \right)^{-1} = m_e (1 + 2\alpha E) \quad (3.5)$$

Therefore, both m_e and α can be determined with the help of Eq. (3.5) from experimental measurements of the carrier effective mass. Note that the traditional definition of the carrier effective mass, $m^* = \hbar^2 (d^2E/dk^2)^{-1}$, is not valid for non-parabolic semiconductors because an assumption of constant, energy independent effective mass was made in the derivation of this relation [11].

For a carrier in state \mathbf{k} with energy $E_i(\mathbf{k})$ in a band labeled by subscript i , the direction averaged band mass $m_i(\mathbf{k})$ associated with electron is given by [12]:

$$\frac{1}{m_i(\mathbf{k})} = \frac{1}{3\hbar^2} \nabla_{\mathbf{k}}^2 E_i(\mathbf{k}) \quad (3.6)$$

The conductivity effective mass, m_c (where c is either e for electrons or h for holes), is the thermal average of this quantity which is determined by [13]:

$$\frac{1}{m_c^*} = \frac{1}{3\hbar^2} \sum_{i,j} f_{T_c}^\mu(E^j(\mathbf{k})) \frac{\partial^2 E^j(\mathbf{k})}{\partial k_i^2} dk \bigg/ \sum_j f_{T_c}^\mu(E^j(\mathbf{k})) dk \quad (3.7)$$

where, $f_{T_c}^\mu(E_j)$ is the Fermi-Dirac distribution function with Fermi level μ (chemical potential) and temperature T_c and $E^j(\mathbf{k})$ is the energy of j th conduction or valence band; the index i is taken over the three principal cubic directions. The solution of Eq. (3.7), according to Eq. (3.1), is given by Riffe [14] as:

$$\frac{1}{m_e(E)} = \frac{1}{m_{e0}} \frac{1 + (8/3)\alpha(E + \alpha E^2)}{[1 + 4\alpha(E + \alpha E^2)]^{3/2}} \quad (3.8)$$

3.2 Empirical Models

For applied high electric fields, the energy of carriers may be far from a band edge and then the variation of $E(\mathbf{k})$ with \mathbf{k} is non-parabolic. The conduction-band non-parabolicity is a result of mixing between states in different bands, especially conduction and valence bands. The energy dependence of the electron effective mass, due to the non-parabolicity, may be described by the following relation [36]:

$$\frac{1}{m_e^*(E)} = \frac{1}{m_e^*(0)} \left(1 + \frac{2K_2 E}{E_g} \right) \quad (3.9)$$

where, E_g is the energy band gap and K_2 is the empirically adjusted parameter. This formula was discussed by Hopkins and the value of K_2 in GaAs is given as -1.75 (in bulk material) and -1.4 (in two-dimensional electron gas) [16].

Another model is given by Hrivnak [17, 18]. He proposed and verified a semi-empirical relation for energy gaps at Γ point of tetrahedral semiconductors. The relation proposed by Hrivnak is used for the calculation of electron and light hole energy levels in quantum wells on the basis of the knowledge of the electron and light hole effective masses, the lattice constant, and the width of the well. This is given by:

$$E_g^\Gamma = (m_e^\Gamma + m_{lh}^\Gamma) c_g^2 \quad (3.10)$$

where, m_e^Γ and m_{lh}^Γ are the values of the electron and light hole effective mass at the Γ point, respectively, and c_g is determined by the ratio:

$$c_g = \frac{2\pi\hbar}{m_0 a} \quad (3.11)$$

with a as the lattice constant.

The temperature dependence of the energy gap in GaAs is calculated according to Eq. (2.1) with $E_g(0)=1.519\text{eV}$, $\alpha=5.405\times 10^{-4}\text{K}^{-1}$, $\beta=204\text{K}$.

$$E_g^\Gamma(T) = 1.519 - \frac{5.405 \times 10^{-4} \text{K}^{-1}}{T + 204\text{K}} T^2 \quad (3.12)$$

The generally accepted value of m_e^Γ/m_0 at very low temperature is 0.0665 which has been experimentally determined by Chamberlain et al. [19] for GaAs. Using the value $m_0 c_g^2 = 9.4\text{eV}$ [$a(\text{GaAs}) = 5.654\text{\AA}$], the temperature dependence of electron and light hole effective masses in GaAs is obtained as:

$$\frac{m_e^\Gamma(T)}{m_0} = m_e^\Gamma(0) - \frac{\alpha_e}{T + \beta} T^2 \quad (3.13)$$

$$\frac{m_{lh}^\Gamma(T)}{m_0} = m_{lh}^\Gamma(0) - \frac{\alpha_{lh}}{T + \beta} T^2 \quad (3.14)$$

The temperature dependent reduced mass m_r can be calculated as:

$$m_r(T) = \frac{c_g^2}{E_g^\Gamma(T)} \left(m_{lh}^\Gamma(0) m_e^\Gamma(0) - \frac{(m_e^\Gamma(0) \alpha_{lh} + m_{lh}^\Gamma(0) \alpha_e)}{T + \beta} T^2 + \frac{\alpha_{lh} \alpha_e}{T + \beta} T^4 \right) \quad (3.15)$$

Eq. (3.15) can be used to calculate the temperature-dependent transmission coefficient which is discussed in Chapter 4. Figure 3.1 shows the temperature dependence of the effective masses in which the green line represents the light hole effective mass, blue line is the electron effective mass and the red dashed line is the reduced effective mass. With increase in temperature, the effective masses decrease slightly. Light hole effective mass decreases faster than electron effective mass. The parameters used in the calculations are as follows: $m_e^\Gamma(0) = 0.0665$, $m_{lh}^\Gamma(0) = 0.0951$, $\alpha_e = 1.848 \times 10^{-5} \text{K}^{-1}$, $\alpha_{lh} = 3.902 \times 10^{-5} \text{K}^{-1}$, $m_0 c_g^2 = 9.4 \text{eV}$, $a(\text{GaAs}) = 5.654 \text{\AA}$, $E_g^\Gamma(0) = 1.519 \text{eV}$, $\alpha = 5.405 \times 10^{-4} \text{K}^{-1}$, $\beta = 204 \text{K}$.

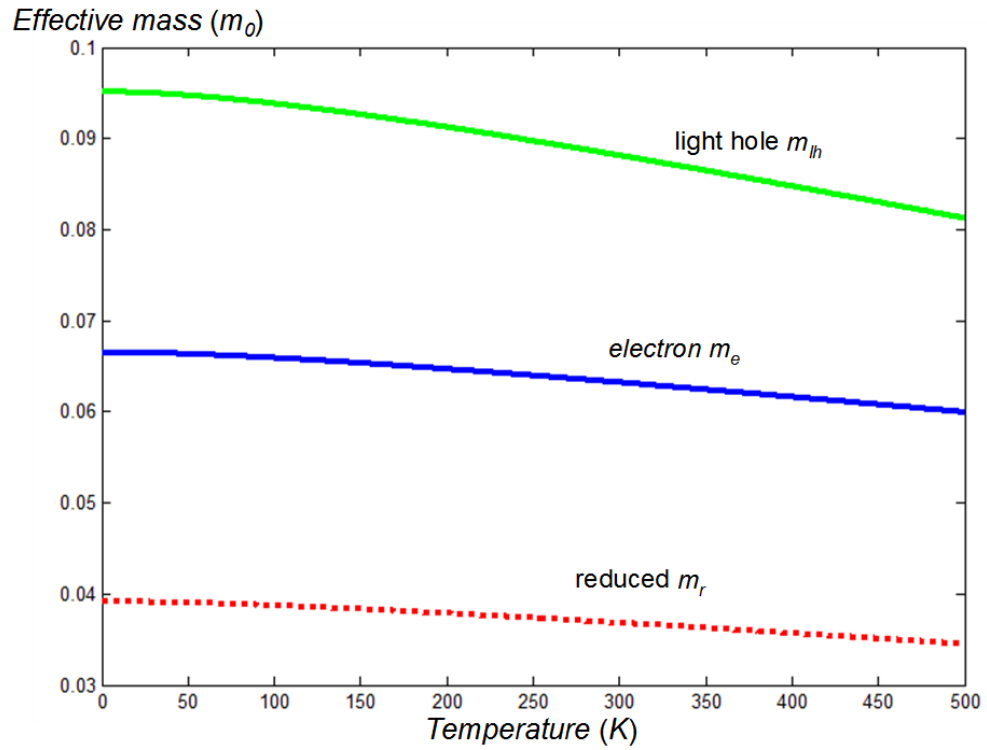


Figure 3.1 Temperature dependence of the effective masses, in GaAs, ranging from 0K to 500K according to Hrivnak's model.

CHAPTER 4

TUNNELING

4.1 Introduction

Quantum-mechanical tunneling in semiconductor diodes was first observed by Zener [21]. Zener tunneling in semiconductor involves transitions between the valence and the conduction band induced by appreciable fields. It is also widely referred to as interband tunneling or band-to-band tunneling (BtBT) and, together with avalanche breakdown caused by impact ionization, it is considered as the working principle of the so-called Zener diodes. More recently, the effect of BtBT has attracted significant research interest due to its impact on device leakage in metal-oxide-semiconductor field-effect transistors (MOSFETs). Tunnel field-effect transistors (FETs) have the potential of achieving sub-threshold swing that is less than the thermal limit in conventional MOSFETs and therefore they have the potential for low-power computing applications [22-26].

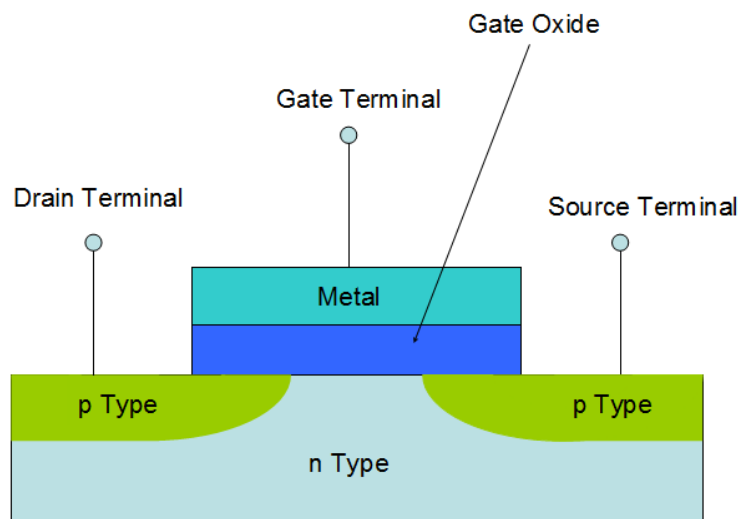


Figure 4.1 Schematic of MOSFET structure.

A MOSFET, shown in Figure 4.1, consists of an n-(p-)doped silicon substrate with two, highly p-(n-)doped contacts, source and drain. The so-called channel region in between is covered by an insulating layer, the gate-oxide, which is in contact with the gate electrode. Without applying a voltage at the gate electrode, no current can flow from source to drain as the pn-junctions between each contact and the substrate act as two opposite diodes. When applying a positive (negative) voltage at the gate electrode, the channel region close to the gate oxide is "inverted" (i.e. from n-(p-) to p-(n-)doped) and current can flow between source and drain.

Over 40 years ago, a theoretical investigation of Zener tunneling was provided by Kane [27] who treated BtBT for direct gap semiconductor subjected to a uniform electric field. In order to obtain a compact formula, he used a two-band $k \cdot p$ model to quantify the band structure, while the transition probabilities were calculated from Fermi's golden rule. The transmission coefficient is given by Kane [28, 29] and can also be obtained by WKB theory [30, 31]. WKB approximation provides such a tool, through which the transmission coefficient can be calculated from the wave vector, which is dependent on the type of barrier. For indirect band gap semiconductors and structures acted upon by non-uniform electric field, Kane's model and the WKB approximation have led to reasonable fits with recent experimental data. The phonon-assisted tunneling plays a significant role in case of silicon and other materials with indirect band gap. Often the barrier for tunneling is considered to be $E_c - E$ [32-36], which is the barrier of electrons, or $E - E_v$ [37], which is the barrier for holes.

In this thesis, a theoretical analysis is shown based on the WKB approximation for tunneling probability combined with effective mass effect and non-parabolic effect. The

temperature dependence of the energy band gap, electron effective mass and light hole effective mass have been investigated based on GaAs in order to deduce the temperature effect on tunneling process. The temperature-dependent complex band structure is investigated. The non-parabolic approximation (NPA) is shown to describe the complex band structure of common semiconductor materials, such as GaAs, in the energy region that is important to BtBT. NPA shows ever more improvement in describing the complex band structure over the parabolic approximation (PA) due to the inherent elliptic nature of the complex bands inside a band gap region [38]. In comparison with parabolic approximation and non-parabolic approximation results, the tunneling probability and current density is found to have a strong dependence on non-parabolicity factor. The tunneling current density function is developed from a series representation for the incomplete gamma function into Tsu-Esaki tunneling current formula with the consideration of the non-parabolic effect and its variation with temperature is also investigated.

4.2 Tunneling Mechanisms

In the silicon-dielectric-silicon structure, sketched in Figure 4.2, a variety of tunneling processes can be identified. Considering the shape of the energy barrier alone, Fowler-Nordheim (FN) tunneling and direct tunneling can be distinguished. However, a more rigorous classification distinguishes between ECB (electrons from the conduction band), EVB (electrons from the valence band), HVB (holes from the valence band), and TAT (trap-assisted tunneling) processes. The EVB process is caused by electrons tunneling from the valence band to the conduction band. It thus creates free carriers on

both sides of the dielectric, which, for MOS transistors, gives rise to increased substrate current. The TAT process can either be elastic, which means that the energy of the carrier is conserved, or inelastic, where the carrier loses energy due to the emission of phonons. Furthermore, in dielectrics with a very high defect density, hopping conduction via multiple defects may occur.

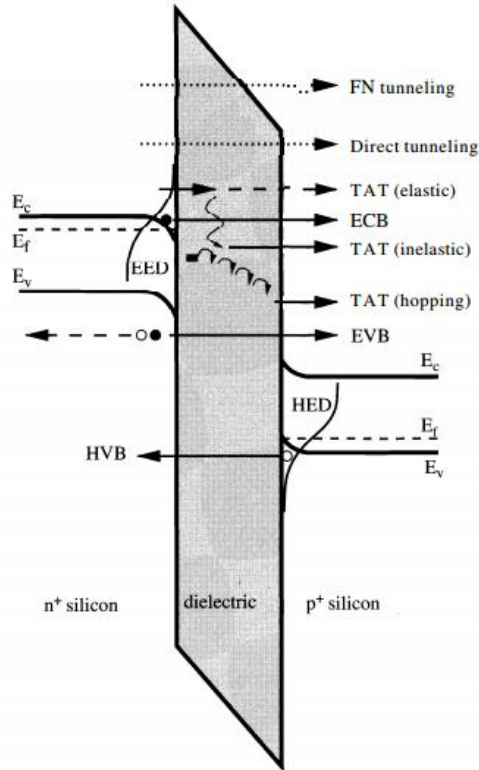


Figure 4.2 Schematic of the tunneling processes in a silicon-dielectric-silicon structure. The different tunneling processes are indicated by arrows and are described in the text. The abbreviations EED and HED denote the electron and hole energy distribution function. [39]

4.3 Band-to-band Tunneling in Diodes

The tunneling of interest in this thesis is band-to-band tunneling in silicon diodes and TFETs. For band-to-band tunneling to occur, the electrons in the valence band of the semiconductor tunnels across the band gap to the conduction band without the assistance

of traps as shown in Figure 4.3.

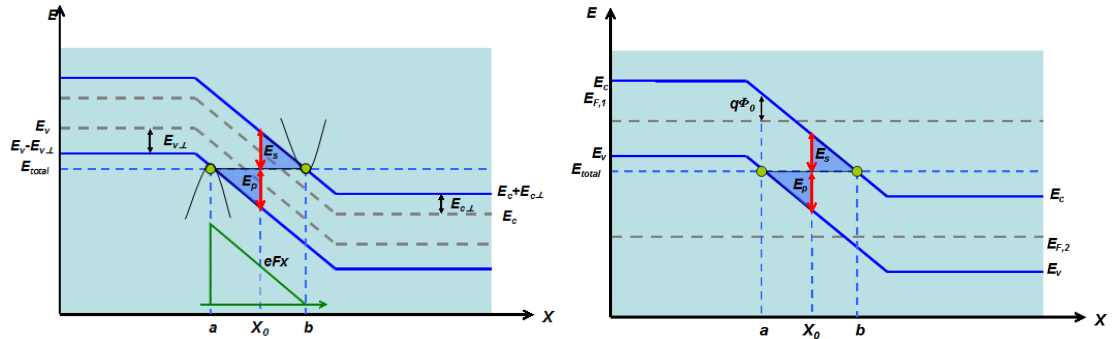


Figure 4.3 Band diagram for the tunneling electrons with nonzero perpendicular momentum in the valence band and conduction band. A particle with nonzero perpendicular momentum tunnels across the band gap from the valence band at $x=a$ to the conduction band at $x=b$. The transition from valence band-like properties to conduction band-like properties occurs at $x=x_0$, and the overall tunneling barrier is indicated by the dark areas. $E_{F,1}$ and $E_{F,2}$ are the Fermi levels on the left side and on the right side respectively. $q\Phi_0$ is the effective barrier height.

Figure 4.3 depicts band-to-band tunneling for a heavily doped p+/n+ diode with a constant electric field across the junction. An incident valence band electron with energy in the x direction tunnels across the band gap to the conduction band. The electron tunnels from the valence band at $x=a$ to the conduction band at $x=b$, and the phonon interaction, for a transition from valence band-like properties to conduction band-like properties, occurs at $x=x_0$. The tunneling barrier is indicated by the hatched areas in the figure.

Assuming that there is no loss of energy during the transition as well as no scattering involved, the energy of the electron ending up in the conduction band should be equal to the sum of its energy at the start of tunneling in the valence band and the gained energy from the acceleration due to the electric field. Electron in the valence band can tunnel to any state in the conduction band such that the total energy and perpendicular momentum are conserved which is shown in the following equation [40]:

$$E_v(0) - \frac{\hbar^2 k^2}{2m_v^*} + qFx + \hbar\omega_\beta = E_c + \frac{\hbar^2 k^2}{2m_c^*} \quad (4.1)$$

$$k_{c\perp} = k_{v\perp} + \beta_\perp \quad (4.2)$$

where, F denotes the electric field and m_c^* and m_v^* are valence and conduction band effective masses respectively. β is the wave vector of the phonon. Under the continuum approximation, β can be any value so that $k_{c\perp}$ is independent of $k_{v\perp}$. Because this energy is quite small, the approximation is made so that no change in the total energy occurs with the phonon interaction, and the term $\hbar\beta$ is neglected.

4.4 Complex Band Structure

4.4.1 Parabolic Approximation

For parabolic band, the dispersion relation in semiconductor is approximated by:

$$E = \frac{\hbar^2 k^2}{2m^*} \quad (4.3)$$

where, m^* is the effective mass. The imaginary part of the wave vector κ with valence band-like properties and conduction band-like properties can be derived respectively as:

$$\kappa_v = \frac{1}{\hbar} \sqrt{2m_v^* E_{vx}} \quad 0 < E_{vx} < E_p, \quad (4.4)$$

$$\kappa_c = \frac{1}{\hbar} \sqrt{2m_c^* (E_g - E_{vx})} \quad E_p < E_{vx} < E_g, \quad (4.5)$$

where, $E_{vx}(x) = E - E_v(x)$, m_c^* and m_v^* are electron and hole effective mass respectively, and E_g is the direct band gap.

4.4.2 Non-parabolic Approximation

The conventional non-parabolic approximation of real band structures can be modified and generalized to approximate the complex band structures of common semiconductors with a significant improvement in accuracy relative to the parabolic approximation. The improvement is due to the inherent elliptic nature of the complex band structures in the vicinity of the band gap, which has a critical impact on the band-to-band tunneling probability [38]. From Kane's two-band $\mathbf{k}\cdot\mathbf{p}$ model, assuming that the conduction band minimum is at $k_0=0$, the electron Hamiltonian in the vicinity of k_0 is:

$$\begin{bmatrix} \frac{\hbar^2 k^2}{2m_0} & \frac{\hbar}{m_0} kp \\ \frac{\hbar}{m_0} kp^* E_g + \frac{\hbar^2 k^2}{2m_0} & \end{bmatrix} \quad (4.6)$$

where, m_0 is the free electron mass, E_g is the energy band gap, and $p = \langle u_{vk_0} | \hat{p} | u_{ck_0} \rangle$ is the Kane's momentum matrix element between two unit cell functions (u_{vk_0} and u_{ck_0}) at band extremes. Assuming that $\hbar^2 k^2 / 2m_0$ is negligible compared to $E(k)$ and letting $E_p = 2|p|^2 / m_0$, the secular equation is:

$$E(k)[E(k) - E_g] = E_p \frac{\hbar^2 k^2}{2m_0} \quad (4.7)$$

For $E(k) > E_g$, the conventional NPA of the conduction band can be obtained by defining $m^* = m_0 E_g / E_p$, $E'(k) = E(k) - E_g$, and $\alpha = 1/E_g$ which is given by [42]:

$$E'(k)[1 + \alpha E'(k)] = \frac{\hbar^2 k^2}{2m^*} \quad (4.8)$$

For BtBT, the energy interest is within $0 < E(k) < E_g$. The solution of Eq. (4.7) therefore results in a complex k . We have $k = i\kappa$ with:

$$\kappa = \frac{1}{\hbar} \sqrt{2m^* E (1 - E/2E_g)} \quad (4.9)$$

and $E_g = E_g/2$. However, for real band structure in which the electrons and holes have different effective masses, the simple two-band model is not valid. E_q is no longer equal to $E_g/2$ with different electron and hole effective mass. It is assumed that the tunneling carriers start propagating through the energy band gap along the hole branch and transition to the electron branch occurs when $E_p(x_0) = E_g m_c^* / (m_c^* + m_v^*)$ [41]. The NPA of complex branches in direct band gap is calculated by:

$$\kappa_v = \frac{1}{\hbar} \sqrt{2m_v^* E_{vx} [1 - E_{vx} / (\beta E_p)]} \quad 0 < E_{vx} < E_p, \quad (4.10)$$

$$\kappa_c = \frac{1}{\hbar} \sqrt{2m_c^*(E_g - E_{vx})[1 - (E_g - E_{vx})/(\beta E_g - \beta E_p)]} \quad E_p < E_{vx} < E_g, \quad (4.11)$$

where, $E_{vx}(x)=E-E_v(x)$, κ is the imaginary part of the wave vector, m_c^* and m_v^* are electron and hole effective mass respectively, and E_g is the direct band gap. β is a parameter that describes the non-parabolicity in dispersion relation.

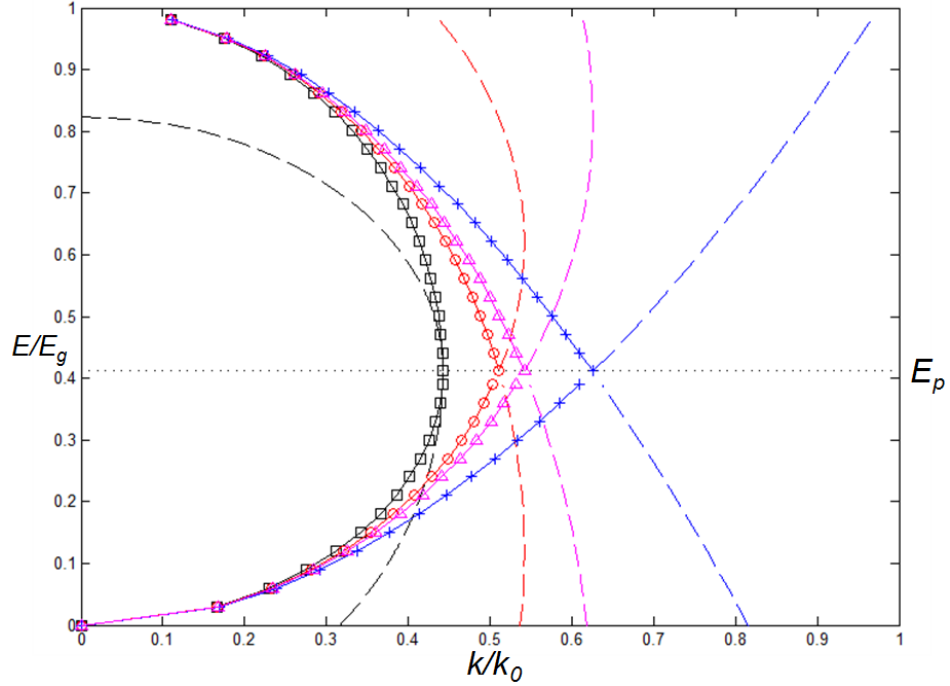


Figure 4.4 Energy vs imaginary wave vector within the band gap according to Eq. (4.10) and Eq. (4.11) and the tunneling path assumed in calculation (solid line) with various values of β . ($\square \beta = 2$, $\circ \beta = 3$, $\Delta \beta = 4$, $+ \beta \rightarrow \infty$). E_g is the energy band gap and E_p is the energy at which the tunneling carriers crossover from the hole branch to the electron branch while transversing through the energy band gap. Parameters used in the calculation: $E_g = 1.52 \text{ eV}$, $m_c^* = 0.06m_0$, $m_v^* = 0.09m_0$; m_0 free electron mass, $k_0 = \hbar^{-1}(2m_0)^{1/2}$.

Figure 4.4 shows the hole branch and electron branch. The crossover point is at E_p which the transition from valence band-like properties to conduction band-like properties occurs. In the limit of $E_{vx} \rightarrow 0^+$, we can find that κ is approaching to $\kappa = \frac{1}{\hbar} \sqrt{2m_v^* E_{vx}}$. In the

limit of $E_{vx} \rightarrow E_g^-$, κ is approaching to $\kappa = \frac{1}{\hbar} \sqrt{2m_c^*(E_g - E_{vx})}$. The complex band structure performs a parabolic behavior near the real band extremes. When $\beta = 2$, the inherent elliptic nature of a complex band is revealed with joint two real bands at their extremes. With increase in β , the PA properties begin to dominate the complex band structure and, in the limit of $\beta \rightarrow \infty$, NPA totally becomes PA of complex band structure.

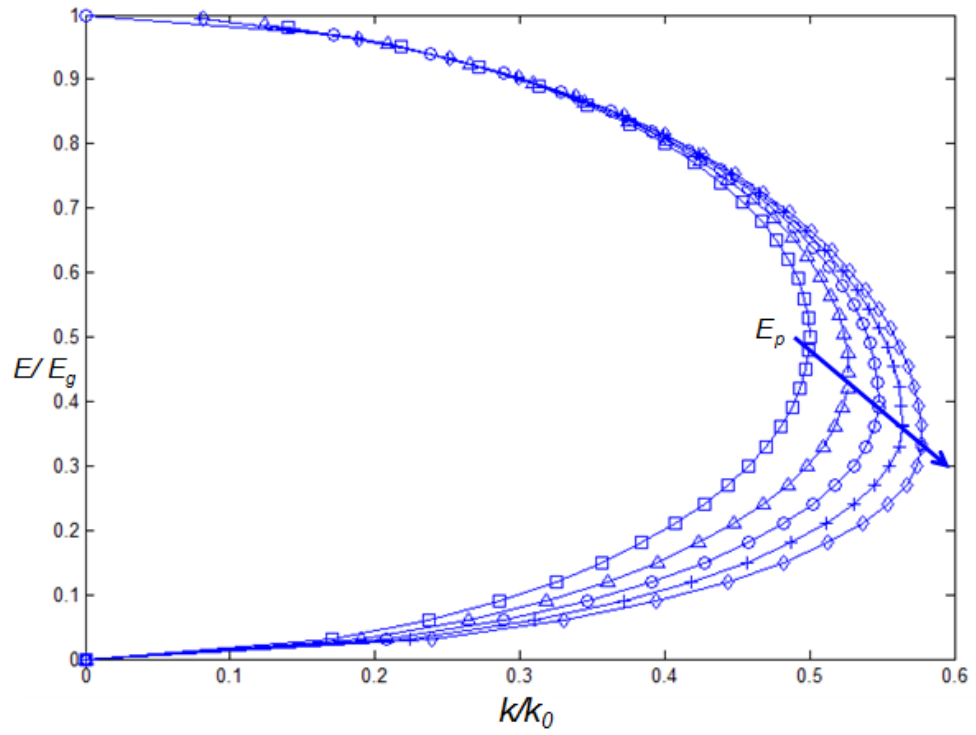


Figure 4.5 Complex band structure for various electron-hole effective mass ratio $\gamma = m_c^*/m_v^*$. ($\square \gamma = 1$, $\Delta \gamma = 1.25$, $\circ \gamma = 1.5$, $+ \gamma = 1.75$, $\diamond \gamma = 2$).

Not only the non-parabolicity factor greatly affects the complex band structure, but also the effective masses dominate the shift in its turning point. Figure 4.5 shows that, with increase in hole effective mass, the crossover point shifts towards the valence band which indicates that the energy E_p is even smaller with a longer tunneling path.

4.5 Tunneling Probability

4.5.1 Transmission Coefficient Modeling

The shape of the energy barrier has been treated as in Figure 4.6; the calculation of the quantum mechanical transmission coefficient can be investigated. The transmission coefficient T is defined as:

$$J(r) = \frac{i\hbar q}{2m} (\Psi \nabla \Psi^* - \Psi^* \nabla \Psi) \quad (4.12)$$

due to an incident wave in Region I and a transmitted wave in Region III as shown in Figure 4.6. The assumption of plane waves in both regions:

$$\Psi_I(x) = A_I \exp(ik_I x) \quad (4.13)$$

$$\Psi_{III}(x) = A_{III} \exp(ik_{III} x) \quad (4.14)$$

leads to the transmission coefficient:

$$T = \frac{J_{III}}{J_I} = \frac{k_I m_I |A_{III}|^2}{k_{III} m_{III} |A_I|^2} \quad (4.15)$$

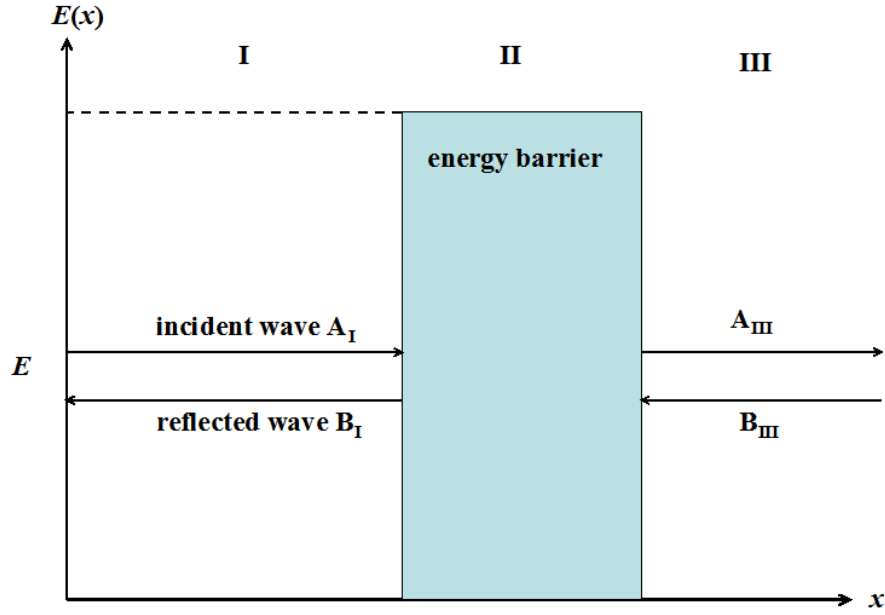


Figure 4.6 Schematic of an energy barrier of a single-layer dielectric. Plane wave is incident on the rectangular potential barrier, a portion of the incident wave is transmitted and the rest is reflected at the energy barrier.

Note that the quantum-mechanical current density Eq. (4.13) is equal in Region I and Region III. Considering only the incident wave in Region I and the transmitted wave in Region II allows the definition of a transmission coefficient $T \leq 1$. The wave function amplitudes A_I , and A_{III} can be found by solving the stationary Schrodinger equation [39]:

$$\left[-\frac{\hbar^2}{2m} \nabla^2 + W(r) \right] \Psi(r) = E \Psi(r) \quad (4.16)$$

where, $W(r)$ is an external potential energy, in the barrier region. This can be achieved by various methods. The Wentzel-Kramers-Brillouin approximation can be applied either analytically for a linear barrier or numerically for arbitrary barriers.

4.5.2 The The Wentzel-Kramers-Brillouin Approximation

The Wentzel-Kramers-Brillouin approximation is one of the most frequently applied approximations to solve the Schrodinger's equation:

$$\left[-\frac{\hbar^2}{2m} \nabla^2 + W(r) - E \right] \Psi(r) = 0 \quad (4.17)$$

The transmission coefficient is give as [43]:

$$T = g \exp(-2 \int_0^a \kappa(x) dx) \quad (4.18)$$

where, g is the prefactor, κ is the imaginary term of the electron wave vector in the barrier, and x is the physical distance across the barrier, $0 < x < a$, where, a is the barrier thickness. k is electron wave vector and, in the forbidden energy gap, k is purely imaginary, so that $\kappa = ik$, $i = \sqrt{-1}$.

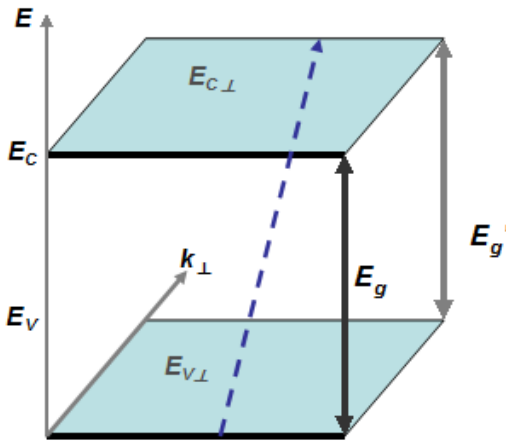


Figure 4.7 E - k plot depicting the increased band gap incurred by perpendicular momentum.

As shown in Figure 4.7, a particle with some perpendicular momentum, $\hbar k_{\perp}$, in the valence band tunnel to the conduction band with the same $\hbar k_{\perp}$. k_{\perp} is the wave vector to the perpendicular direction.

Thus,

$$\begin{aligned} k_v^2 &= k_{vx}^2 + k_{v\perp}^2 & k_{vx}^2 &= k_v^2 - k_{v\perp}^2 \\ k_c^2 &= k_{cx}^2 + k_{c\perp}^2 & k_{cx}^2 &= k_c^2 - k_{c\perp}^2 \end{aligned} \quad (4.19)$$

Let $\kappa_x = ik_x$, $\kappa_v = ik_v$, $\kappa_c = ik_c$, thus $\kappa_{vx} = \sqrt{(\kappa_v^2 + k_{v\perp}^2)}$, $\kappa_{cx} = \sqrt{(\kappa_c^2 + k_{c\perp}^2)}$.

The tunneling probability can be rewritten in terms of the total momentum and perpendicular momentum $\hbar k_{\perp}$ as:

$$T = \exp \left[-2 \left(\int_a^{x_0} (\kappa_v^2 + k_{v\perp}^2) dx + \int_{x_0}^b (\kappa_c^2 + k_{c\perp}^2) dx \right) \right] \quad (4.20)$$

This equation can be simplified by first factoring κ_v and κ_c out of the square root and then applying the Taylor series approximation that $\sqrt{1+\alpha} \approx 1+\alpha/2$, for $\alpha \ll 1$, as:

$$T = \exp \left[-2 \left(\int_a^{x_0} \kappa_v dx + \int_{x_0}^b \kappa_c dx \right) - \left(k_{v\perp}^2 \int_a^{x_0} \kappa_v^{-1} dx + k_{c\perp}^2 \int_{x_0}^b \kappa_c^{-1} dx \right) \right] \quad (4.21)$$

If the perpendicular momentum in the valence band and conduction band is zero, the integral of $\kappa(x)$ can be written in terms of E_{vx} as:

$$T = \exp \left[-2 \left(\int_a^{x_0} \kappa_v dx + \int_{x_0}^b \kappa_c dx \right) \right] = \exp \left[-\frac{2}{qF} \left(\int_0^{E_p} \kappa_v dE_{vx} + \int_{E_p}^{E_g} \kappa_c dE_{vx} \right) \right] \quad (4.22)$$

where, $E_{vx}(x)=E-E_v(x) = E-(E_{v0}.eFx)$ and $dE_{vx}=qFdx$. F is the electric field which is assumed to be a positive constant. Substituting Eq. (4.19) into Eq. (4.22), the transmission coefficient of NPA can be written as:

$$T = \exp \left[-\frac{2}{qF\hbar} \int_0^{E_p} \sqrt{2m_v^* E_{vx} [1 - E_{vx} (\beta E_p)^{-1}] } dE_{vx} - \frac{2}{qF\hbar} \int_{E_p}^{E_g} \sqrt{2m_c^* (E_g - E_{vx}) [1 - (E_g - E_{vx}) (\beta E_g - \beta E_p)^{-1}] } dE_{vx} \right] \quad (4.23)$$

Let $E_{vx}(\beta E_p)^{-1}=Z_v$, and $(E_g - E_{vx})(\beta E_g - \beta E_p)^{-1}=Z_c$, leading to:

$$T = \exp \left\{ -\frac{2}{qF\hbar} (2m_v^*)^{1/2} (\beta E_p)^{3/2} \int_0^{\beta^{-1}} \sqrt{Z_v [1 - Z_v]} dZ_v - \frac{2}{qF\hbar} (2m_c^*)^{1/2} [\beta (E_g - E_p)]^{3/2} \int_0^{\beta^{-1}} \sqrt{Z_c [1 - Z_c]} dZ_c \right\} \quad (4.24)$$

Finally, from Eq. (4.24), an analytical formula for the transmission coefficient of NPA is derived as:

$$T_{NPA} = \exp \left\{ -\frac{(2\beta)^{3/2}}{4qF\hbar} \left\{ (\beta - 1)^{1/2} \beta^{-2} - (\beta - 1)^{3/2} \beta^{-2} - \arctan \sqrt{\beta - 1} + \frac{\pi}{2} \right\} E_g^{3/2} \sqrt{m_r} \right\} \quad (4.25)$$

where, m_r is the reduced mass (tunneling effective mass) given by $m_v^* m_c^* (m_v^* + m_c^*)^{-1}$.

Eq. (4.25) reveals a non-parabolicity-dependent transmission coefficient. In order to investigate the variation of transmission coefficient with β , the prefactor is quite important which is defined as:

$$\delta = \frac{(2\beta)^{3/2}}{4qF\hbar} \left\{ (\beta-1)^{1/2} \beta^{-2} - (\beta-1)^{3/2} \beta^{-2} - \arctan \sqrt{\beta-1} + \frac{\pi}{2} \right\} \quad (4.26)$$

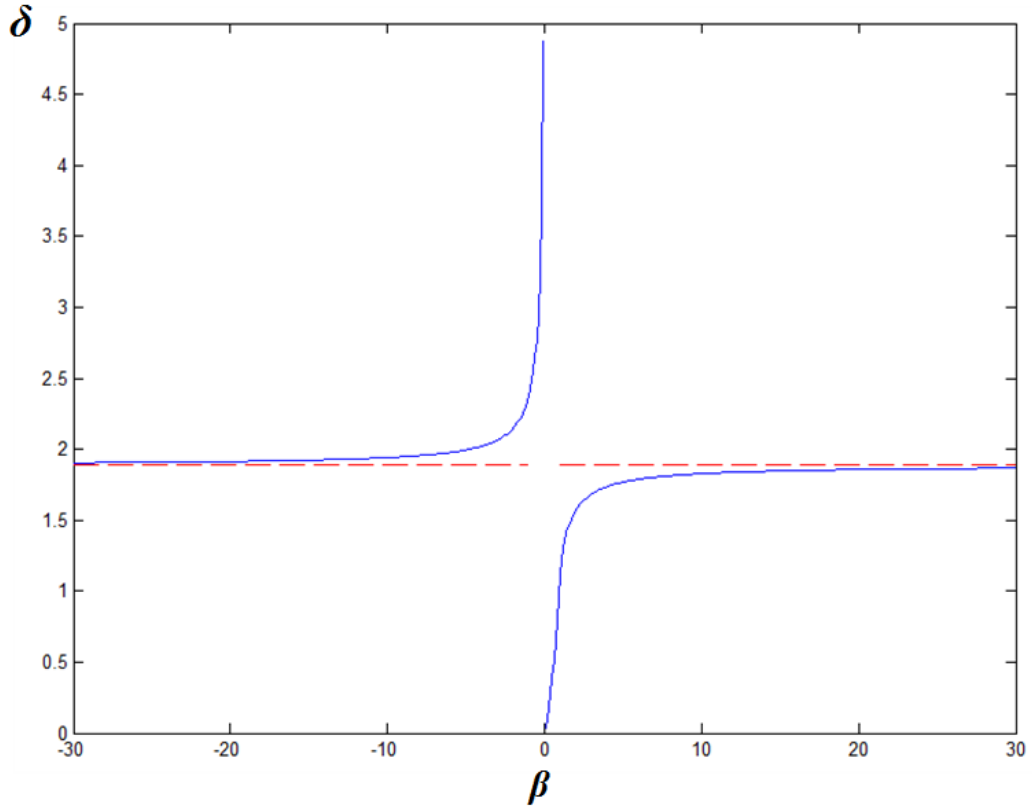


Figure 4.8 The value of prefactor δ according to Eq. (4.26) for the variation of β .

The relation of δ and β is shown in Figure 4.8. As $\beta \rightarrow +\infty$ or $\beta \rightarrow -\infty$, the value of δ approaches a constant, 1.885, which is $4\sqrt{2}/3$. The transmission coefficient of NPA has a limit of minimum as:

$$T_{NPA,\infty} = \exp\left(-\frac{4\sqrt{2}}{3qF\hbar} E_g^{3/2} \sqrt{m_r}\right) \quad (4.27)$$

$$T_{NPA,\infty} = T_{PA} \quad (4.28)$$

which is the transmission coefficient of PA. The transmission coefficient increases as the portion of parabolic behavior of complex band structure decreases.

4.5.3 Temperature-dependent Transmission Coefficient

The temperature-dependent transmission coefficient can be calculated from Eq.(4.25):

$$T_{NPA} = \exp\left\{-\delta E_g^{3/2}(T) \sqrt{m_r(T)}\right\} \quad (4.29)$$

The temperature-dependent reduced mass m_r and energy band gap E_g have been calculated in Chapter 2 and Chapter 3.

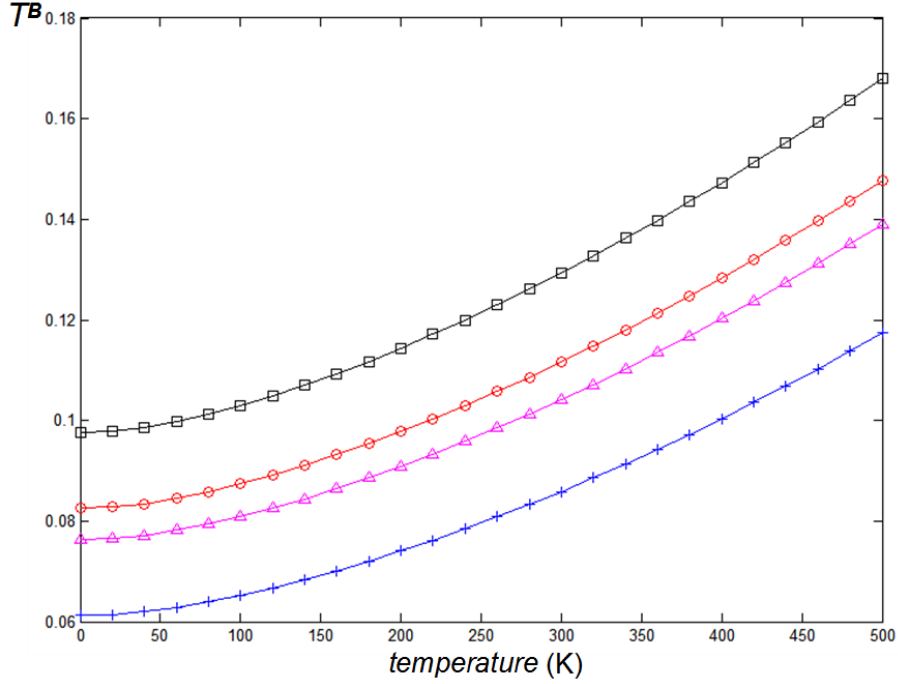


Figure 4.9 Temperature-dependent transmission coefficient of NPA with various values of β . ($\square \beta=2$, $\circ \beta=3$, $\Delta \beta=4$, $+ \beta \rightarrow \infty$). T^B is tunneling probability T with an index of B which is defined as $B=qF\hbar$, q is elementary electric charge, F is electric field, and \hbar is reduced Planck constant.

As is shown in Eq. (4.29), the transmission coefficient can be divided into two parts, the non-parabolic-dependent part δ , and the temperature-dependent part $E_g^{3/2} m_r^{1/2}$. Figure 4.9 shows the total effects. With increase in temperature, the transmission coefficient also increases. As the non-parabolicity factor β increases, it is shifted towards the low probability and tends to be a constant which is given by Eq. (4.27) when β approaches infinity.

4.6 Tunneling Current Density

4.6.1 The Density of States

The density of states function is used to describe how many quantum states are available in the band per unit energy interval. Thus, for a three-dimensional electron distribution,

the density of states can be defined as $g_{3d} = dN_{3d} / dE$ where, $N_{3d}(E)$ is the number of quantum states with energy less than E . For an isotropic semiconductor, constant energy surfaces represent spheres in k space. In a material with the lattice constant a , each volume element of size $(2\pi/a)^3$ is occupied by two quantum states (one for each direction of spin). Counting all states within a sphere of radius k and dividing by a^3 leads to $N_{3D}(k) = k^3 / 3\pi^2$. Then, for non-parabolic band, the density of states is [44]:

$$\begin{aligned} g_{3d} &= \frac{1}{3\pi^2} \frac{d(k^3)}{dE} \\ &= \frac{\sqrt{2}}{\pi^2} \left(\frac{m}{\hbar^2} \right)^{3/2} E^{1/2} (1 + \alpha E)^{1/2} (1 + 2\alpha E) \end{aligned} \quad (4.30)$$

For parabolic band, the density of states is:

$$g_{3d} = \frac{\sqrt{2}}{\pi^2} \left(\frac{m}{\hbar^2} \right)^{3/2} E^{1/2} \quad (4.31)$$

4.6.2. The Tsu-Esaki Model

The tunneling current is usually written as an integral over the product of two independent parts, which only depend on the energy perpendicular to the interface: the transmission coefficient T and the supply function N :

$$J = \frac{qm}{2\pi^2 \hbar^3} \int_{E_{\min}}^{E_{\max}} T(E_x) N(dE_x) dE_x \quad (4.32)$$

which is known as Tsu-Esaki formula [45,48].

In the derivation of Tsu-Esaki Model with non-parabolic approximation, three assumptions are made. The first assumption is Effective-mass approximation: the different masses corresponding to the band structure of the considered material are lumped into a single value for the effective mass. The second assumption is PA and the last assumption is conservation of parallel momentum, that is, only transitions in the x -direction are considered. This model has been proposed by Duke and was used by Tsu and Esaki for the modeling of tunneling current in resonant tunneling devices. When electrons tunnel from the valence band, E_{min} is the lowest conduction band edge and E_{max} is the highest valence band edge.

The net tunnel current density from Electrode 1 to Electrode 2 can be written as the net difference between current flowing from Side 1 to Side 2 and vice versa:

$$J = J_{1 \rightarrow 2} - J_{2 \rightarrow 1} \quad (4.33)$$

The current density through the two interfaces depends on the perpendicular component of the wave vector k_x , the transmission coefficient T , the perpendicular velocity v_x , the density of states g , and the distribution function at both sides of the barrier:

$$dJ_{1 \rightarrow 2} = qT(k_x)v_x g_1(k_x) f_1(E) [1 - f_2(E)] dk_x \quad (4.34)$$

$$dJ_{2 \rightarrow 1} = qT(k_x)v_x g_2(k_x) f_2(E) [1 - f_1(E)] dk_x \quad (4.35)$$

$f_1(E)$ is the probability of Electrode 1 being occupied by electrons and $[1-f_2(E)]$ is the probability of Electrode 2 being vacant. In this expression, it is assumed that the transmission coefficient depends only on the momentum perpendicular to the interface. The density of k_x states $g(k_x)$ is given by:

$$g(k_x) = \int_0^\infty \int_0^\infty g(k_x, k_y, k_z) dk_y dk_z \quad (4.36)$$

where, $g(k_x, k_y, k_z)$ denotes the three-dimensional density of states in the momentum space. Considering the quantized wave vector components within a cube of side length L , each position in k -space being filled with a cubic unit cell volume of $V=(2\pi/L)^3$,

$$(k_x, k_y, k_z) = \left(n_x \frac{2\pi}{L}, n_y \frac{2\pi}{L}, n_z \frac{2\pi}{L} \right) \quad (4.37)$$

The density of states within the cube yields:

$$g(k_x, k_y, k_z) = 2 \frac{1}{k_x k_y k_z} \frac{1}{L^3} = \frac{1}{4\pi^3} \quad (4.38)$$

where, the factor 2 is spin degeneracy. For the non-parabolic dispersion relation, the velocity and energy component in the tunneling direction obey:

$$v_x = \frac{1}{\hbar} \frac{\partial E_x}{\partial k_x} = \frac{\hbar k_x}{m} (1 + 2\alpha E_x)^{-1} \quad (4.39)$$

Hence, Eq. (4.34) and Eq. (4.35) become:

$$dJ_{1 \rightarrow 2} = \frac{q}{4\pi^3 \hbar} T(k_x) dE_x \int_0^\infty \int_0^\infty f_1(E) [1 - f_2(E)] dk_y dk_z = qT(k_x) dE_x n_{1 \rightarrow 2}(p_x) \quad (4.40)$$

$$dJ_{2 \rightarrow 1} = \frac{q}{4\pi^3 \hbar} T(k_x) dE_x \int_0^\infty \int_0^\infty f_2(E) [1 - f_1(E)] dk_y dk_z = qT(k_x) dE_x n_{2 \rightarrow 1}(p_x) \quad (4.41)$$

where,

$$n(p_{i \rightarrow j}) = \frac{1}{4\pi^3 \hbar^3} \int_0^\infty \int_0^\infty f_i(E) (1 - f_j(E)) dp_z dp_y \quad (4.42)$$

Integration of expression Eq. (4.42) can be performed in polar coordinates. Using polar coordinates for the parallel wave vector components,

$$p_r^2 = p_y^2 + p_z^2, \quad p_y = p_r \cos \theta, \quad p_z = p_r \sin \theta \quad (4.43)$$

$$E_r (1 + \alpha E_r) = \frac{p_r^2}{2m}, \quad p_r dp_r = m(1 + 2\alpha E_r) dE_r \quad (4.44)$$

and the total energy E_t according to the non-parabolic dispersion relation yields:

$$E_t(1 + \alpha E_t) = \frac{p_r^2 + p_x^2}{2m}, \quad E_x(1 + \alpha E_x) = \frac{p_x^2}{2m} \quad (4.45)$$

hence,

$$E_t(1 + \alpha E_t) = E_x(1 + \alpha E_x) + E_r(1 + \alpha E_r) \quad (4.46)$$

$$E_t + \frac{1}{2\alpha} = \sqrt{\left(E_x + \frac{1}{2\alpha}\right)^2 + \left(E_r + \frac{1}{2\alpha}\right)^2} - \frac{1}{4\alpha^2} \quad (4.47)$$

The non-parabolic dispersion relation implies that, at the bottom of the band with a parabolic relation, $E \approx \hbar^2 k^2 / 2m$ is preserved, while a small, non-parabolic correction αE^2 is observed for higher E . The total energy can be expressed as $E_t = E_r + E_x$ when the product of α , E_r and E_x is small enough.

Thus, we get:

$$\begin{aligned} n_{i \rightarrow j} &= \frac{1}{4\pi^3 \hbar^3} \int_0^{2\pi} \int_0^\infty f_i(E)(1 - f_j(E)) p_r dp_r d\theta \\ &= \frac{m}{2\pi^2 \hbar^3} \int_0^\infty f_i(E)[1 - f_j(E)](1 + 2\alpha E_r) dE_r \end{aligned} \quad (4.48)$$

and

$$\xi_i = \int_0^\infty \frac{1}{1+e^t} (1+2\alpha E_r) dE_r \quad (4.49)$$

where, $t = (E_x + E_r - E_{F,i})/k_B T$, ζ_i is composed of two Fermi-Dirac integrals. The selected Fermi-Dirac integrals are summarized in Appendix [46]. The solutions of the two integrals are given, respectively, by:

$$\int_0^\infty \frac{1}{1+e^t} dE_r = \left[E_r - k_B T \ln(e^t + 1) \right]_0^\infty = k_B T \ln \left[\exp \left(\frac{E_{F,i} - E_x}{k_B T} \right) + 1 \right] \quad (4.50)$$

$$2\alpha \int_0^\infty \frac{E_r}{1+e^t} dE_r = 2\alpha (k_B T)^2 \left[\int_0^\infty \frac{t}{e^t + 1} dt - \int_0^{\frac{E_x - E_{F,i}}{k_B T}} \frac{t}{e^t + 1} dt \right] + (E_{F,i} - E_x) \int_0^\infty \frac{t}{e^t + 1} dE_r \quad (4.51)$$

Thus,

$$\begin{aligned} \xi_i = & \left[1 + 2\alpha (E_{F,i} - E_x) \right] k_B T \ln \left(e^{\frac{E_{F,i} - E_x}{k_B T}} + 1 \right) + 2\alpha k_B T (E_x - E_{F,i}) \ln \left(e^{\frac{E_x - E_{F,i}}{k_B T}} + 1 \right) \\ & - \alpha (E_x - E_{F,i})^2 + 2\alpha (k_B T)^2 \left[\frac{\pi^2}{6} + Li_2 \left(-e^{\frac{E_x - E_{F,i}}{k_B T}} \right) \right] \end{aligned} \quad (4.52)$$

The supply function N through the barrier is $N = n_{1 \rightarrow 2} - n_{2 \rightarrow 1}$,

$$N(E_x) = \xi_1 - \xi_2 = \int_0^\infty [f_1(E) - f_2(E)](1 + 2\alpha E_r) dE_r \quad (4.53)$$

$$N(E_x) = \left[1 + 2\alpha(E_{F,i} - E_x)\right] k_B T \ln \left(\frac{1 + e^{\frac{E_{F,1} - E_x}{k_B T}}}{1 + e^{\frac{E_{F,2} - E_x}{k_B T}}} \right) + 2\alpha(E_x - E_{F,i}) k_B T \ln \left(\frac{1 + e^{\frac{E_x - E_{F,i}}{k_B T}}}{1 + e^{\frac{E_x - E_{F,j}}{k_B T}}} \right) \quad (4.54)$$

$$+ \alpha(2E_x - E_{F,1} - E_{F,2})(E_{F,1} - E_{F,2}) + 2\alpha(kT_B)^2 \left[\text{Li}_2 \left(-e^{\frac{E_x - E_{F,1}}{k_B T}} \right) - \text{Li}_2 \left(-e^{\frac{E_x - E_{F,2}}{k_B T}} \right) \right]$$

Evaluating the difference $J = J_{1 \rightarrow 2} - J_{2 \rightarrow 1}$, the net current through the interface equals,

$$J = \frac{qm}{2\pi^2 \hbar^3} \int_{E_{\min}}^{E_{\max}} T(E_x) dE_x \int_0^\infty (f_1(E) - f_2(E)) dE_r \quad (4.55)$$

4.6.3 Supply Function Modeling

$N(E)$ is the supply function that describes the difference in the supply of carriers. With parabolic dispersion relation, it is given by [47]:

$$N(E_x) = \int_0^\infty [f_1(E) - f_2(E)] dE_r \quad (4.56)$$

with non-parabolic dispersion relation,

$$N(E_x) = \int_0^\infty [f_1(E) - f_2(E)](1 + 2\alpha E_r) dE_r \quad (4.57)$$

where, f_1 and f_2 denote the energy distribution function near the interfaces. Since the exact form of these distributions is usually not known, approximate shapes are commonly used, and furthermore, it is assumed that the distributions are isotropic.

4.6.4 Fermi-Dirac Distribution

In equilibrium, the energy distribution function of electrons and holes is given by the Fermi-Dirac statistics:

$$f(E) = \frac{1}{1 + \exp\left(\frac{E - E_F}{k_B T}\right)} \quad (4.58)$$

The integral of f is:

$$\int f(E) = \int \frac{1}{1 + \exp\left(\frac{E - E_F}{k_B T}\right)} dE \quad (4.59)$$

and it can be integrated analytically using:

$$\int \frac{1}{1 + \exp(x)} dx = \ln\left(\frac{1}{1 + \exp(-x)}\right) + C \quad (4.60)$$

Thus, the total supply function Eq. (4.56) becomes:

$$N(E) = k_B T \ln \left(\frac{1 + \exp\left(-\frac{E - E_{f,1}}{k_B T}\right)}{1 + \exp\left(-\frac{E - E_{f,2}}{k_B T}\right)} \right) \quad (4.61)$$

4.6.5 Tunneling Current Density Function

The Tsu-Esaki model for the calculation of tunneling currents requires a considerable computational effort. However, for practical device simulation, it is desirable to use compact models that do not require large computational resources.

In order to find a simple approximation of Eq. (4.52):

$$\begin{aligned} \xi_i &= \int_0^\infty \frac{1}{1 + e^t} (1 + 2\alpha E_r) dE_r \quad (4.62) \\ &= [1 + 2\alpha(E_{F,i} - E_x)] k_B T \ln \left(e^{\frac{E_{F,i} - E_x}{k_B T}} + 1 \right) + 2\alpha k_B T (E_x - E_{F,i}) \ln \left(e^{\frac{E_x - E_{F,i}}{k_B T}} + 1 \right) \\ &\quad - \alpha (E_x - E_{F,i})^2 + 2\alpha (k_B T)^2 \left[\frac{\pi^2}{6} + Li_2 \left(-e^{-\frac{E_x - E_{F,i}}{k_B T}} \right) \right] \end{aligned}$$

to avoid numerical integration, as a first approximation, $T \rightarrow 0$ is assumed. The Fermi function $f(x)$ can be replaced by a step function [39]:

$$f_1(E) = f_1(E - E_{F,1}) = \begin{cases} 1 & (E \leq E_{F,1}) \\ 0 & (E > E_{F,1}) \end{cases} \quad (4.63)$$

$$f_1(E) = f_1(E - E_{F,2}) = \begin{cases} 1 & (E \leq E_{F,2}) \\ 0 & (E > E_{F,2}) \end{cases}$$

Without loss of generality, it can be assumed that $E_{F,1} > E_{F,2}$. The innermost integral can then be evaluated analytically for three distinct regions:

When $E > E_{F,1}$, $f_1(E - E_{F,1}) = 0$, $f_2(E - E_{F,2}) = 0$,

$$N = 0 \tag{4.64}$$

When $E_{F,2} < E < E_{F,1}$, $f_1(E - E_{F,1}) = 1$, $f_2(E - E_{F,2}) = 0$,

$$N \approx \xi_1 = (E_{F,1} - E) + 3\alpha(E_{F,1} - E)^2 \tag{4.65}$$

When $E < E_{F,2}$, $f_1(E - E_{F,1}) = 1$, $f_2(E - E_{F,2}) = 1$,

$$N \approx \xi_1 - \xi_2 = (E_{F,1} - E_{F,2}) + 3\alpha[(E_{F,1} - E)^2 - (E_{F,2} - E)^2] \tag{4.66}$$

Hence,

$$N = \begin{cases} (E_{F,1} - E_{F,2}) + 3\alpha[(E_{F,1} - E)^2 - (E_{F,2} - E)^2] & (E \leq E_{F,2}) \\ (E_{F,1} - E) + 3\alpha(E_{F,1} - E)^2 & (E_{F,2} \leq E \leq E_{F,1}) \\ 0 & (E_{F,1} < E) \end{cases} \tag{4.67}$$

This leads to the following expression for the current density:

$$J = \frac{qm}{2\pi^2\hbar^3} \int_{-\infty}^{E_{F,2}} T(E) \left\{ (E_{F,1} - E_{F,2}) + 3\alpha \left[(E_{F,1} - E)^2 - (E_{F,2} - E)^2 \right] \right\} dE \quad (4.68)$$

$$+ \frac{qm}{2\pi^2\hbar^3} \int_{E_{F,2}}^{E_{F,1}} T(E) \left\{ (E_{F,1} - E) + 3\alpha (E_{F,1} - E)^2 \right\} dE$$

The first integral represents tunneling current from electron states that are low in energy and face a high energy barrier. Hence, as a second approximation, the first integral is neglected. By inserting the expression of transmission coefficient from Eq. (4.67) in the second integral, the current density becomes:

$$J = \sigma \int_{E_{F,2}}^{E_{F,1}} \exp(\delta E_g^{3/2}(E)) \left\{ (E_{F,1} - E) + 3\alpha (E_{F,1} - E)^2 \right\} dE \quad (4.69)$$

where,

$$\delta = -\frac{(2\beta)^{3/2} \sqrt{m_r}}{qF\hbar} \left\{ (\beta-1)^{1/2} \beta^{-2} - (\beta-1)^{3/2} \beta^{-2} - \arctan \sqrt{\beta-1} + \frac{\pi}{2} \right\}, \quad \sigma = \frac{qm}{2\pi^2\hbar^3} \quad \text{and}$$

$E_g(E) = q\Phi_0 + E_{F,1} - E$ with $dE_g(E) = -dE$. Let $E_g(E) = \chi$ in order to simplify the expressions. Eq. (4.69) can be written as $J=J_1+J_2$ with:

$$J_1 = \sigma \int_{q\Phi_0 + E_{F,1} - E_{F,2}}^{q\Phi_0} \exp(\delta \chi^{3/2}) (q\Phi_0 - \chi) d\chi \quad (4.70)$$

$$= \sigma q\Phi_0 \int_{q\Phi_0 + E_{F,1} - E_{F,2}}^{q\Phi_0} \exp(\delta \chi^{3/2}) d\chi - \sigma \int_{q\Phi_0 + E_{F,1} - E_{F,2}}^{q\Phi_0} \exp(\delta \chi^{3/2}) \chi d\chi$$

$$\begin{aligned}
J_2 &= 3\alpha\sigma \int_{q\Phi_0+E_{Fn}-E_{Fp}}^{q\Phi_0} \exp(\delta\chi^{3/2})(q\Phi_0 - \chi)^2 d\chi \\
&= 3\alpha\sigma(q\Phi_0)^2 \int_{q\Phi_0+E_{Fn}-E_{Fp}}^{q\Phi_0} \exp(\delta\chi^{3/2}) d\chi - 6\alpha q\Phi_0\sigma \int_{q\Phi_0+E_{Fn}-E_{Fp}}^{q\Phi_0} \exp(\delta\chi^{3/2}) \chi d\chi \\
&\quad + 3\alpha\sigma \int_{q\Phi_0+E_{Fn}-E_{Fp}}^{q\Phi_0} \exp(\delta\chi^{3/2}) \chi^2 d\chi
\end{aligned} \tag{4.71}$$

and its solution is:

$$\begin{aligned}
J_1 &= \sigma q\Phi_0 \left[\frac{2}{3} \delta^{-2/3} (-1)^{1/3} \Gamma\left(\frac{2}{3}, -\delta\chi^{3/2}\right) \right]_{q\Phi_0+E_{Fn}-E_{Fp}}^{q\Phi_0} \\
&\quad - \sigma \left[\frac{2}{3} \delta^{-1} \chi^{1/2} e^{\delta\chi^{3/2}} - \frac{2}{9} \delta^{-4/3} (-1)^{2/3} \Gamma\left(\frac{1}{3}, -\delta\chi^{3/2}\right) \right]_{q\Phi_0+E_{Fn}-E_{Fp}}^{q\Phi_0}
\end{aligned} \tag{4.72}$$

$$\begin{aligned}
J_2 &= 3\alpha\sigma(q\Phi_0)^2 \left[\frac{2}{3} \delta^{-2/3} (-1)^{1/3} \Gamma\left(\frac{2}{3}, -\delta\chi^{3/2}\right) \right]_{q\Phi_0+E_{Fn}-E_{Fp}}^{q\Phi_0} \\
&\quad + 3\alpha\sigma \left[\frac{2e^{\delta\chi^{3/2}}}{3\delta^2} (\delta\chi^{3/2} - 1) \right]_{q\Phi_0+E_{Fn}-E_{Fp}}^{q\Phi_0} \\
&\quad - 6\alpha\sigma q\Phi_0 \left[\frac{2}{3} \delta^{-1} \chi^{1/2} e^{\delta\chi^{3/2}} - \frac{2}{9} \delta^{-4/3} (-1)^{2/3} \Gamma\left(\frac{1}{3}, -\delta\chi^{3/2}\right) \right]_{q\Phi_0+E_{Fn}-E_{Fp}}^{q\Phi_0}
\end{aligned} \tag{4.73}$$

where, $\Gamma(a,x)$ is the "upper" incomplete gamma function which is given by:

$$\Gamma(a, x) \equiv \int_x^\infty t^{a-1} e^{-t} dt \tag{4.74}$$

The widely used asymptotic series representations for the incomplete gamma function is [49, 50]:

$$\Gamma(a, x) \approx x^{a-1} e^{-x} \left[1 + \frac{a-1}{x} + \frac{(a-1)(a-2)}{x^2} + \dots \right] \quad (4.75)$$

and by inserting this expression in Eq. (4.72) and Eq. (4.73) with the low-order terms neglected, yields:

$$J_1 = \frac{2}{3} \sigma e^{\delta \chi^{3/2}} \left\{ \begin{array}{l} \delta^{-1} (q\Phi_0 \chi^{-1/2} - \chi^{1/2}) + \frac{1}{3} \delta^{-2} (q\Phi_0 \chi^{-2} + \chi^{-1}) \\ + \frac{4}{9} \delta^{-3} (q\Phi_0 \chi^{-7/2} + \chi^{-5/2}) + \frac{2}{27} \delta^{-4} (14q\Phi_0 \chi^{-5} + 5\chi^{-4}) \end{array} \right\} \Bigg|_{q\Phi_0 + E_{Fn} - E_{Fp}}^{q\Phi_0} \quad (4.76)$$

$$J_2 = 2\alpha \sigma e^{\delta \chi^{3/2}} \left\{ \begin{array}{l} \delta^{-1} [(q\Phi_0)^2 \chi^{-1/2} - 2q\Phi_0 \chi^{1/2} + \chi^{3/2}] \\ + \frac{1}{3} \delta^{-2} [(q\Phi_0)^2 \chi^{-2} + 2q\Phi_0 \chi^{-1} - 3] \\ + \frac{4}{9} \delta^{-3} [(q\Phi_0)^2 \chi^{-7/2} + q\Phi_0 \chi^{-5/2}] \end{array} \right\} \Bigg|_{q\Phi_0 + E_{Fn} - E_{Fp}}^{q\Phi_0} \quad (4.77)$$

Hence, the current density yields:

$$\begin{aligned}
J_1 = & \frac{4}{9} \sigma e^{\delta(q\Phi_0)^{3/2}} \delta^{-2} (q\Phi_0)^{-1} + \frac{16}{27} \sigma e^{\delta(q\Phi_0)^{3/2}} \delta^{-3} (q\Phi_0)^{-5/2} \\
& - \frac{2}{3} \sigma e^{\delta(q\Phi_0+\Delta)^{3/2}} \delta^{-1} [q\Phi_0 (q\Phi_0 + \Delta)^{-1/2} - (q\Phi_0 + \Delta)^{1/2}] \\
& - \frac{2}{9} \sigma e^{\delta(q\Phi_0+\Delta)^{3/2}} \delta^{-2} [(q\Phi_0 + \Delta)^{-1} + q\Phi_0 (q\Phi_0 + \Delta)^{-2}] \\
& - \frac{8}{27} \sigma e^{\delta(q\Phi_0+\Delta)^{3/2}} \delta^{-3} [q\Phi_0 (q\Phi_0 + \Delta)^{-7/2} + (q\Phi_0 + \Delta)^{-5/2}]
\end{aligned} \tag{4.78}$$

$$\begin{aligned}
J_2 = & \frac{16}{9} \alpha \sigma \delta^{-3} e^{\delta \chi^{3/2}} (q\Phi_0)^{-3/2} \\
& - 2\alpha \sigma e^{\delta \chi^{3/2}} \delta^{-1} [(q\Phi_0)^2 (q\Phi_0 + \Delta)^{-1/2} - 2(q\Phi_0)(q\Phi_0 + \Delta)^{1/2} + (q\Phi_0 + \Delta)^{3/2}] \\
& - \frac{2}{3} \alpha \sigma e^{\delta \chi^{3/2}} \delta^{-2} [(q\Phi_0)^2 (q\Phi_0 + \Delta)^{-2} + 2(q\Phi_0)(q\Phi_0 + \Delta)^{-1} - 3] \\
& - \frac{8}{9} \alpha \sigma e^{\delta \chi^{3/2}} \delta^{-3} [(q\Phi_0)^2 (q\Phi_0 + \Delta)^{-7/2} + (q\Phi_0)(q\Phi_0 + \Delta)^{-5/2}]
\end{aligned} \tag{4.79}$$

where, $\Delta = E_{F,1} - E_{F,2}$.

The direct BtBT current in field-induced p-n junction can be calculated according to Eq. (4.78) and Eq. (4.79). Under conditions of thermal equilibrium, Δ is zero that cannot lead to BtBT current flow. But when a reverse bias voltage is applied, an energy window is open over which the current flows. When the applied voltage is much smaller than the band gap, the resulting field due to the voltage is only a small fraction of the built-in electric field at the junction; the extra field can be neglected.

However, with increase in applied voltage, the change in the electric field must be considered. If we already know the built-in voltage, we get the electric field:

$$F \propto \sqrt{q\Psi_0 + \Delta} \quad (4.80)$$

$$F = F_0 \sqrt{\frac{q\Psi_0 + \Delta}{q\Psi_0}} \quad (4.81)$$

Consider the effective mass and band gap of GaAs as reference at 300K with $E_g=1.4225\text{eV}$, $m_e=0.0632m_0$, $m_{lh}=0.0881m_0$. Set $qF=1\text{eV/m}$, $\hbar=6.58\times 10^{-16}\text{eV}\cdot\text{s}$, $E_{Fn}=0.4\text{eV}$, $q\Phi_0=1.06\text{eV}$ and σ as a constant; the current density J of parabolic band structure and non-parabolic band structure versus Δ is shown in Figure 4.10.

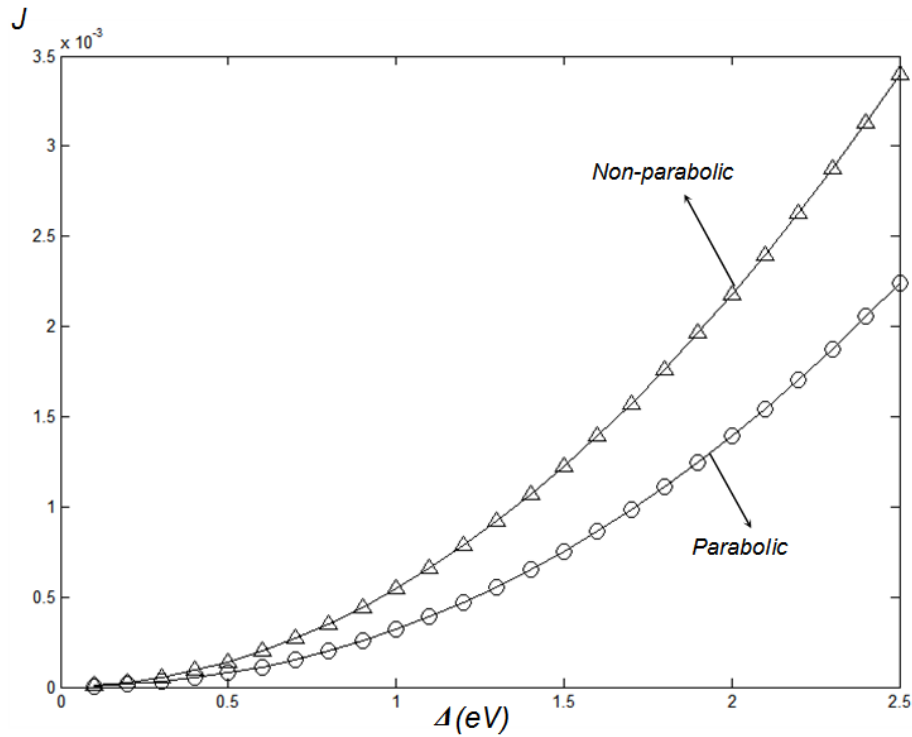


Figure 4.10 The current density J of parabolic band structure and non-parabolic band structure versus Δ .

Figure 4.10 reveals that the non-parabolic band structure has a higher tunneling current density than the parabolic band structure.

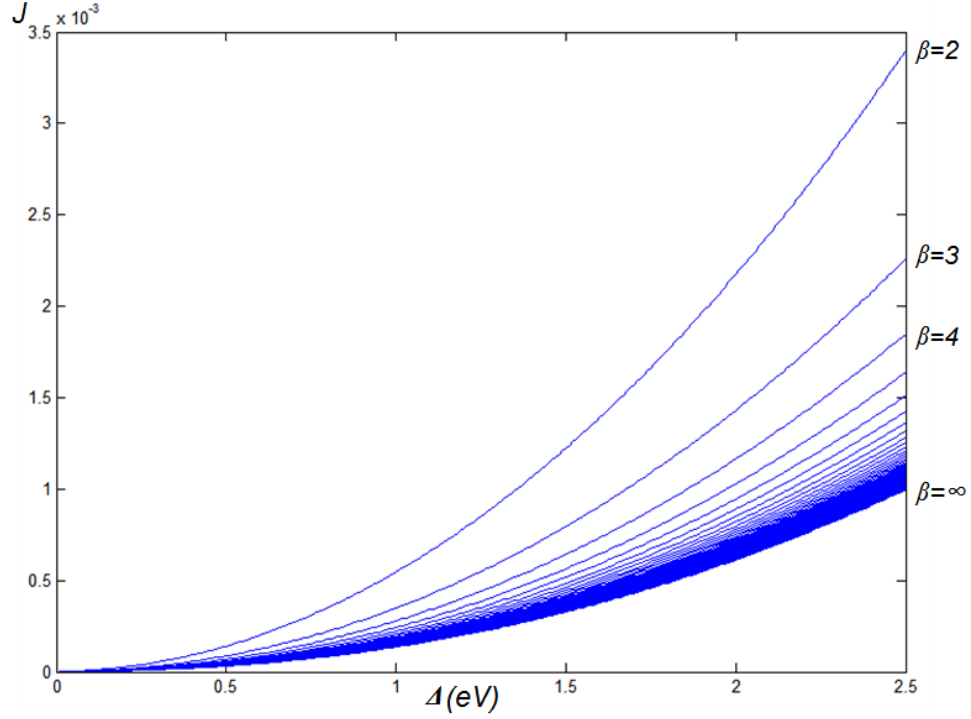


Figure 4.11 The current density J with various β .

The relation between the non-parabolicity factor β and α is $\alpha = -1/(\beta E_q)$; $E_q = E_g m_c / (m_c + m_v)$. The tunneling current is minimum when $\beta \rightarrow \infty$, $\alpha \rightarrow 0$, which is shown in Figure 4.11. As the non-parabolicity factor β increases or α decreases, the ratio of non-parabolic behavior of the complex bands decreases which indicates that the non-parabolic correction αE^2 is decreasing. When $\alpha \rightarrow 0$, J_2 becomes zero and the tunneling current is only contributed from the parabolic behavior of the complex band.

The direct BtBT current J with the variation of Δ is shown in Figure 4.10 and Figure 4.11. Assuming $\Delta \gg q\Phi_0$, the terms which contain $e^{\delta(q\Phi_0 + \Delta)^{3/2}}$ can be neglected and the current density becomes:

$$J = \frac{4}{9} \sigma e^{\delta(q\Phi_0)^{3/2}} \delta^{-2} (q\Phi_0)^{-1} + \frac{16}{27} \sigma e^{\delta(q\Phi_0)^{3/2}} \delta^{-3} (q\Phi_0)^{-5/2} - \frac{16}{9} \alpha \sigma \delta^{-3} e^{\delta \chi^{3/2}} (q\Phi_0)^{-3/2} \quad (4.82)$$

With parabolic dispersion relation and neglecting the higher order terms, for a further approximation, Eq. (4.82) reduces to:

$$J = \frac{4}{9} \sigma e^{\delta(q\Phi_0)^{3/2}} \delta^{-2} (q\Phi_0)^{-1} \quad (4.83)$$

which is the equation commonly known as the Fowler-Nordheim formula.

4.6.6 Temperature-dependent Tunneling Current Density

Considering that the total energy E also changes with temperature, the temperature dependent effective barrier height $q\Phi_0$ yields:

$$q\Phi_0 = E_g(T) - E_{Fn} + E(T) \quad (4.84)$$

E_{Fn} is assumed as a constant and the total energy E is approximated by the thermal energy with the kinetic term being neglected which can be written as $E = 1/2m^*v^2 + 3/2k_B T_C \approx 3/2k_B T_C$, where, m^* , v , and T_C are the effective electron mass, electron velocity, and electron temperature, respectively, k_B is the Boltzmann constant [51]. Hence, Eq. (4.84) can be written as:

$$q\Phi_0 = E_g(T) - E_{Fn} + \frac{3}{2} k_B \alpha T \quad (4.85)$$

α is a parameter characterizing the relation between the electron temperature in the plane

parallel to the junction interface and the device temperature ($\alpha=T_C/T$). When electrons are in the equilibrium state, α should be 1. Recall that the Fermi function is a step function. At $T=0$, the energy levels will be completely filled up to the certain energy which is called Fermi energy and there will be no occupied states with the energy higher than Fermi energy. However, as the temperature is increased, the Fermi function smears out so that the step function is not accurate at high temperature. The energy band gap E_g and reduced mass m_r are temperature-dependent which is already calculated above so that δ can be modified as a function of temperature T .

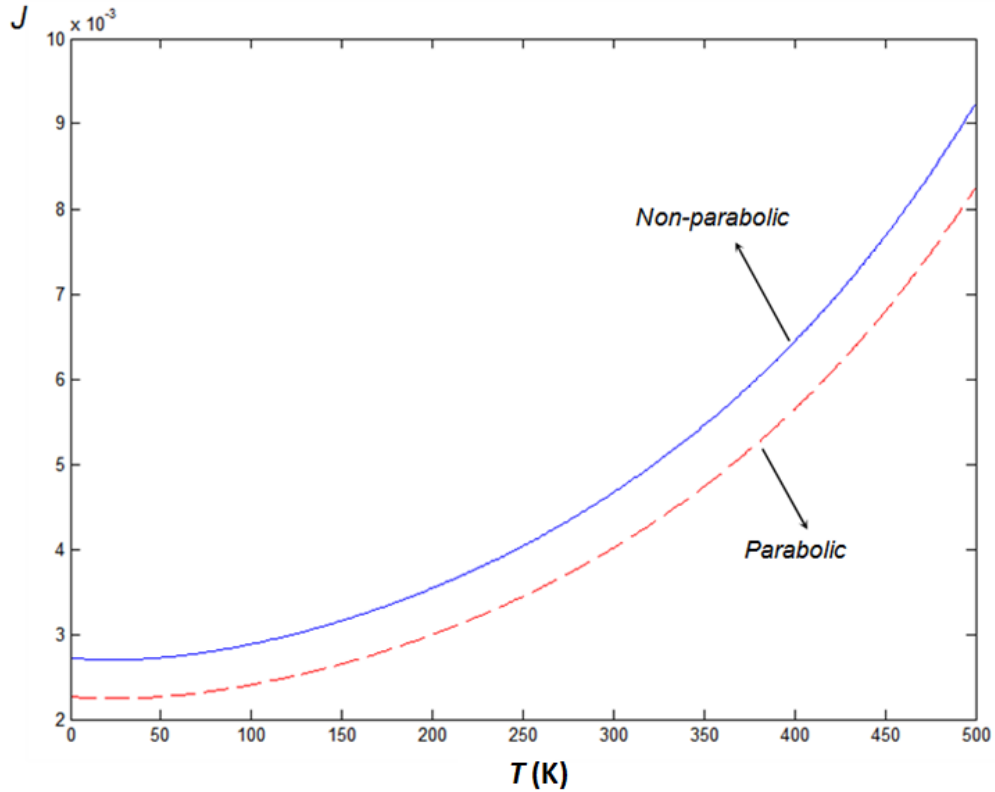


Figure 4.12 Temperature dependent tunneling current density is calculated according to Eq. (2.1) with Eq. (3.15). Parameters used in calculation: $\beta=2$, $E_{Fn}=0.9\text{eV}$, $E_{Fp}=0.1\text{eV}$, $qF=1\text{eV}/\mu\text{m}$, $\hbar=6.58\times 10^{-16}\text{eV}\cdot\text{s}$, $m_0=9.1\times 10^{-31}\text{kg}$, $m_e^r(0)=0.0665$, $m_{lh}^r(0)=0.0951$, $\alpha_e=1.848\times 10^{-5}\text{K}^{-1}$, $\alpha_{lh}=3.902\times 10^{-5}\text{K}^{-1}$, $m_0c_g^2=9.4\text{eV}$, $a(\text{GaAs})=5.654\text{\AA}$, $E_g^r(0)=1.519\text{eV}$, $\alpha=5.405\times 10^{-4}\text{K}^{-1}$, $\beta_{E_g}=204\text{K}$. The tunneling current density of parabolic band and non-parabolic band is almost parallel with the temperature increase from 0K to 500K.

CHAPTER 5

QUANTUM EFFICIENCY MODEL – APPLICATION TO SOLAR CELLS

5.1 Introduction

A solar cell is an electronic device which directly converts sunlight into electricity via the photovoltaic effect. Light incident on the solar cell produces both a current and a voltage to generate electric power. This process requires firstly, a material in which the absorption of light raises an electron to a higher energy state, and secondly, the movement of this higher energy electron from the solar cell into an external circuit. The electron then dissipates its energy in the external circuit and returns to the solar cell. A variety of materials and processes can potentially satisfy the requirements for photovoltaic energy conversion, but, in practice, nearly all photovoltaic energy conversion uses semiconductor materials in the form of a $p-n$ junction.

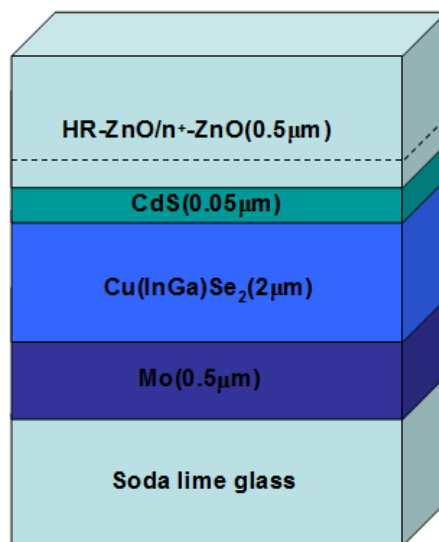
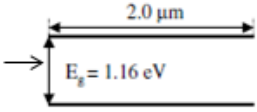
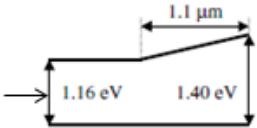
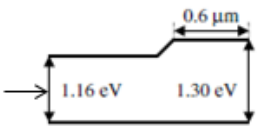
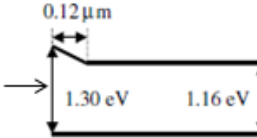
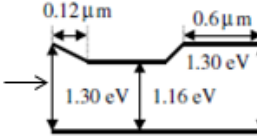
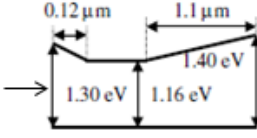


Figure 5.1 Schematic cross section of a typical Cu(InGa)Se_2 solar cell.

Figure 5.1 shows a cross-sectional schematic of a Cu(InGa)Se₂ solar cell. This structure utilizes a soda lime glass substrate, coated with a sputtered Mo layer as a back contact. After Cu(InGa)Se₂ deposition, the junction is formed by chemical bath-deposited CdS with thickness ≤ 50 nm. Then a high-resistance (HR) ZnO layer and a doped high-conductivity ZnO layer are deposited, usually by sputtering or chemical vapor deposition [52].

In this Chapter, device modeling and simulation studies of a Cu(In_{1-x}Ga_x)Se₂ (CIGS) thin film solar cell have been carried out. A variety of graded band-gap structures, as shown in Table 5.1, including space charge region (SCR) grading, back surface region grading, and double grading of the CIGS absorber layer have been considered. Introducing a grading in the absorber can improve cell performance [53] and some modern CIGS solar cells have such a graded band gap profile [54]. It is difficult to discern the real benefit of grading, as varying material properties through the cell implies changing the mean value of the studied parameter, and it is almost impossible to produce a reference cell having the same properties as the studied cell. Hence, if one wants to study grading properties thoroughly, one should use numerical simulations. Several authors have already performed simulations of graded solar cells [55-60].

Table 5.1 CIGS Solar Cells With Various Absorber Band Gap Profiles

	Band-gap profile	η (%)	V_{oc} (mV)	J_{sc} (mA/cm ²)	FF (%)
Case 1		15.42	617	34.05	73.4
Case 2		15.72	622	34.61	73.1
Case 3		15.81	620	34.77	73.3
Case 4		17.57	658	33.55	79.6
Case 5		18.34	669	34.46	79.6
Case 6		18.39	675	34.31	79.4
Case 7	Same profile as Case 6	19.83	688	34.42	83.8

An optimal graded band-gap profile, such as a double grading consisting of SCR grading and back surface grading, improves the efficiency significantly [61]. A new world record efficiency of Cu(In,Ga)Se₂ thin-film solar cells is 20.3% [62].

5.2 Photon Energy and Flux

Light travels at speed c in vacuum which has a frequency f and a wavelength λ .

Frequency can be related to the wavelength by the speed of light in the equation:

$$c = \lambda f \quad (5.1)$$

The energy of a photon, as described in “The Basics of Quantum Theory”, is given by the equation:

$$E = hf \quad (5.2)$$

$$E = \frac{hc}{\lambda} \quad (5.3)$$

The higher the frequency, shorter is the wavelength, and the greater the energy of the photon.

Photon flux is another important concept because it allows us to understand how much light actually comes into contact with devices on the surface of the earth, and therefore how many electrons can be generated for current flow. Flux is a fancy word for the amount of something coming into contact with or passing through a given surface area. Therefore, the photon flux is just the amount of photons incident on the surface of a solar cell in a given time. The photon flux is given by the equation:

$$\Phi = \frac{Number_{photons}}{Area} \quad (5.4)$$

where, Φ is the photon flux, $Number_{photons}$ is the number of photons per second and $Area$ is in square meters.

5.3 Generation Rate

The generation rate gives the number of electrons generated at each point in the device due to the absorption of photons. Generation is an important parameter in solar cell operation.

Neglecting reflection, the amount of light which is absorbed by a material depends on the absorption coefficient (α in cm^{-1}) and the thickness of the absorbing material. The intensity of light at any point in the device can be calculated according to the equation:

$$I = I_0 e^{-\alpha x} \quad (5.5)$$

where, α is the absorption coefficient typically in cm^{-1} , x is the distance into the material at which the light intensity is being calculated and I_0 is the light intensity at the top surface.

The equation can be used to calculate the number of electron-hole pairs being generated in a solar cell. Assuming that the loss in light intensity (i.e., the absorption of photons) directly causes the generation of an electron-hole pair, the generation G in a thin slice of material is determined by finding the change in light intensity across this slice. Consequently, differentiating the above equation will give the generation at any point in the device:

$$G = \alpha \Phi_0 e^{-\alpha x} \quad (5.6)$$

where, Φ_0 = photon flux at the surface, α = absorption coefficient and x = distance into

the material. The above equations show that the light intensity exponentially decreases throughout the material and the generation is highest at the surface of the material. For photovoltaic applications, the incident light consists of a combination of many different wavelengths, and, therefore, the generation rate at each wavelength is different. The generation rate at different wavelengths in silicon is shown below.

5.4 Absorption Coefficient

5.4.1 Absorption Coefficient with Urbach Tail

The absorption coefficient determines how far into a material light of a particular wavelength can penetrate before it is absorbed. In a material with a low absorption coefficient, light is only poorly absorbed, and if the material is thin enough, it will appear transparent to that wavelength. The absorption coefficient depends on the material and also on the wavelength of light being absorbed.

The absorption coefficient α is composed of two parts. When $h\nu < E_g + E_U/2$, weak sub-bandgap absorption takes place, α is proportional to $\exp\left[\left(h\nu - E_g\right)/E_U\right]$. When $h\nu > E_g + E_U/2$, stronger absorption takes place and α is proportional to $\sqrt{h\nu - E_g}$ [83]. E_U is the characteristic Urbach band-tail energy and E_g is band gap energy. The Urbach tail dominates absorption near but below the band gap and further below the band gap is dominated by free-carrier absorption [63].

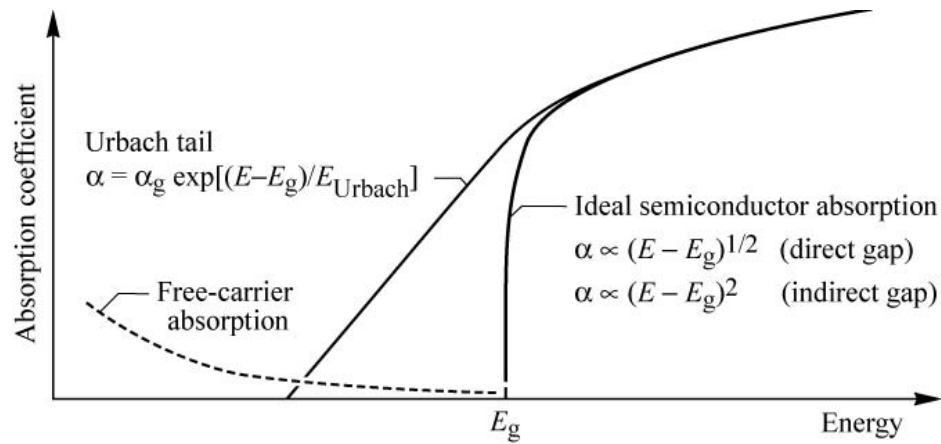


Figure 5.2 Absorption coefficient of a semiconductor with band gap E_g versus energy. [64]

5.4.2 Urbach Energy

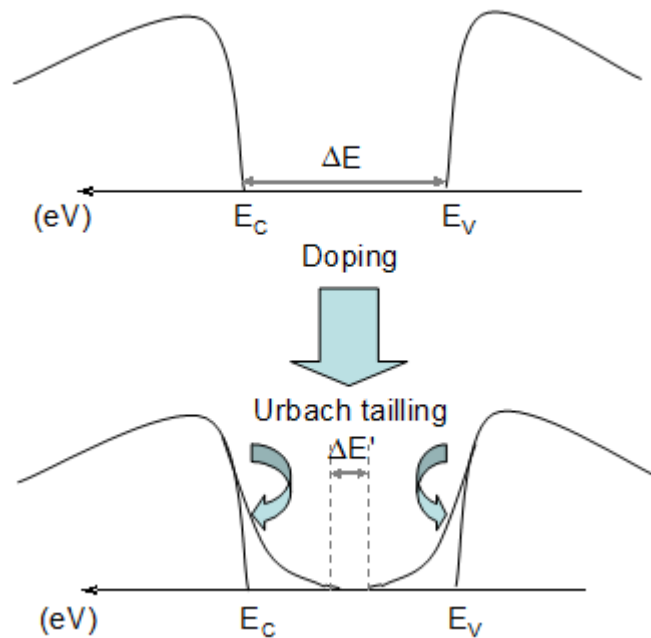


Figure 5.3 Urbach tail occurrence scheme.

Urbach tail can be a telltale signature of the presence of impurities and disorder [65]. Urbach tail is due to the broadening of the exciton absorption band which occurs when charged impurities in the lattice induce phonon-induced micro-electric fields.

The exponential conduction-band (CBT) model developed by Grein [66] assumed that a “transport edge” E_c exists within the electron density, $g(E)$, of the conduction band. In some amorphous semiconductors, such as a-Si:H, the absorption is dominated by a single band tail. CBT model denotes that the absorption is dominated by the conduction band tail. The electron does not interact with phonons; thus no valence-band tail forms in its approximation. Ionic crystals, other insulators, crystalline semiconductors, and amorphous semiconductors show experimental tails in the energy dependence of the optical absorption.

$$\alpha = \alpha_0 \exp\left(\frac{h\nu - E_F}{E_U}\right) \quad (5.7)$$

E_U is the Urbach energy which represents the width of the exponential tail, E_F is the energy of the Urbach focus which coincides roughly with the energy of the lowest free exciton at zero lattice temperature. The width E_U appears to have additive contributions from thermal origin, E_{th} , and structure origin, E_{st} [67]. For high quality crystalline semiconductors, E_U is a direct measure of the temperature-induced disorder, while for amorphous or highly doped materials, E_U becomes larger because of the contributions from both thermal and structural (topological) disorders.

$$E_U = E_{th} + E_{st} = k \left[\langle U^2 \rangle_T \right] + k \left[\langle U^2 \rangle_X \right] \quad (5.8)$$

U is mean square displacement (also called thermal shifting) of the atoms in an alloy that arises from both static and dynamic disorder. The first term represents the contribution of electron/exciton-phonon interaction like the Debye-Waller factor and the second term is due to the mean-square deviation of atoms, caused by the structural disorder, from a perfectly ordered lattice.

The width of the exponential tail E_U , in long wavelength, can be described by the form $E_U = kT/\sigma + W_s$, where the steepness parameter [68]:

$$\sigma = \sigma_0 \left(\frac{2kT}{h\nu_p} \right) \tanh(h\nu_p / 2kT) \quad (5.9)$$

W_s describes the broadening of the edge due to the static (defect induced) disorder, $W_d = kT/\sigma$ describes the broadening by the dynamic (phonon induced) disorder. The temperature dependence of E_{th} is linear above the Debye temperature Θ , then dropping rapidly at Θ and passing over to power law variation at low temperature, clearly implicating phonons. E_{st} increases with the structure disorder, implying that E_{th} arises from the instantaneous thermal disorder introduced by phonons.

E_U can be modelled as an Einstein oscillator which takes into account contributions of dynamic thermal, static structural and compositional disorders. According to this model, the Urbach energy can be expressed by:

$$E_U = [E_U(T) + E_U(X, C)] = A \left(e^{\Theta/T} - 1 \right)^{-1} + B \quad (5.10)$$

where, A and B are constants related to thermal, structural and compositional disorders. Θ , the Einstein temperature, is the same as that discussed earlier in the temperature dependence of the band gap. Cody [69] explained a similar variation of E_U in α -Si using an empirical relation of a modified version of Eq. (5.10):

$$E_U(T, X) = \frac{k\Theta}{\sigma_0} \left[\frac{(1+X)}{2} + \frac{1}{e^{\Theta/T} - 1} \right] \quad (5.11)$$

X is an adjustable parameter related to the structural disorder. The value of Θ is obtained from a theoretical fit of the temperature dependence of E_g using the Manoogian-Wolley relation [70]. σ_0 varies from 0.7 for highly ionic crystals such as NaCl to about 4 for InAs. Its value for CdS is 2.2. For single crystals (low X values) of CdS, E_U is 11.9meV at 300K and 5.1meV at 77K. The effect of disorder, caused by radiation and excessive doping, on the experimental value of X has been reported in the literature. For highly copper-doped CdS films, X can be large as 32-58 [71].

The $E_g(T)$ behavior is compared with the model proposed by Manoogian and Woolley [72]. This is described by:

$$E_g(T) = E_g(0) - UT^s - V\Theta[\coth(\Theta/2T) - 1] \quad (5.12)$$

where, $E_g(0)$ is the band gap energy at 0K, the second term represents the effect of the lattice thermal dilation, and the third term is related to the electron-phonon interaction [73]. U , s , V and Θ are adjustable parameters nearly independent of temperature [74, 75].

Θ is the frequency of phonon excitation which is approximately related to the Debye temperature Θ_D through $\Theta \approx (3/4)\Theta_D$.

5.5 Quantum Efficiency

The quantum efficiency (QE) is the ratio of the number of carriers collected by the solar cell to the number of photons of a given energy incident on the solar cell. The quantum efficiency may be given either as a function of wavelength or as energy. If all photons of a certain wavelength are absorbed and the resulting minority carriers are collected, then the quantum efficiency at that particular wavelength is unity. The quantum efficiency for photons with energy below the band gap should be zero theoretically. However, because of the existence of Urbach tail, photons can also be absorbed with energy below the band gap.

There are two types of quantum efficiency of a solar cell that are often considered. External quantum efficiency (EQE) is the ratio of the number of charge carriers collected by the solar cell to the number of photons of a given energy incident on the solar cell from outside (incident photons). Internal quantum efficiency (IQE) is the ratio of the number of charge carriers collected by the solar cell to the number of photons of a given energy that shine on the solar cell from outside and are absorbed by the cell.

5.6 Quantum Efficiency Model

5.6.1 The Position-dependent Absorption Coefficient

Considering both absorption processes, Mattheis [76] developed a model to describe the absorptance; the absorption coefficient α is modeled by Kichartz [77] as follows:

$$\begin{aligned}\alpha(h\nu < E_g + E_U/2) &= A\sqrt{\frac{E_U}{2}} \exp\left(\frac{h\nu - E_U/2 - E_g}{E_U}\right) \\ \alpha(h\nu \geq E_g + E_U/2) &= A\sqrt{h\nu - E_g}\end{aligned}\tag{5.13}$$

where, A is a constant for fundamental absorption in a direct band gap semiconductor. When photon energies are even slightly above the band gap, band-tail absorption superposes with direct absorption in a direct band gap semiconductor. The value $h\nu = E_g + E_U/2$ is to fulfill the requirement that $\alpha(h\nu)$ is a continuous and derivable function. However, the exact value of the transition energy corresponding to tail to band absorption has not been determined precisely [78].

The generation rate at distance x from the surface is:

$$G(x, h\nu) = -\alpha(x, h\nu)\phi(x, h\nu)\tag{5.14}$$

$G(x, h\nu)$ can also be described as photon flux $\Phi(x, h\nu)$ in unit depth [79]:

$$G(x, h\nu) = -\frac{\partial\phi(x, h\nu)}{\partial x}\tag{5.15}$$

According to Eq. (5.14) and Eq. (5.15), we obtain a differential equation for the photon flux $\Phi(x, h\nu)$ using a position-dependent absorption coefficient $\alpha(x, h\nu)$:

$$\frac{\partial\phi(x, h\nu)}{\partial x} = -\alpha(x, h\nu)\phi(x, h\nu)\tag{5.16}$$

5.6.2 Modeling of Double-graded Band Gap Structure – Application to Solar Cells

We consider the double-graded band gap structure; the solar cell is modeled by two linearly graded regions as shown in Figure 5.4.

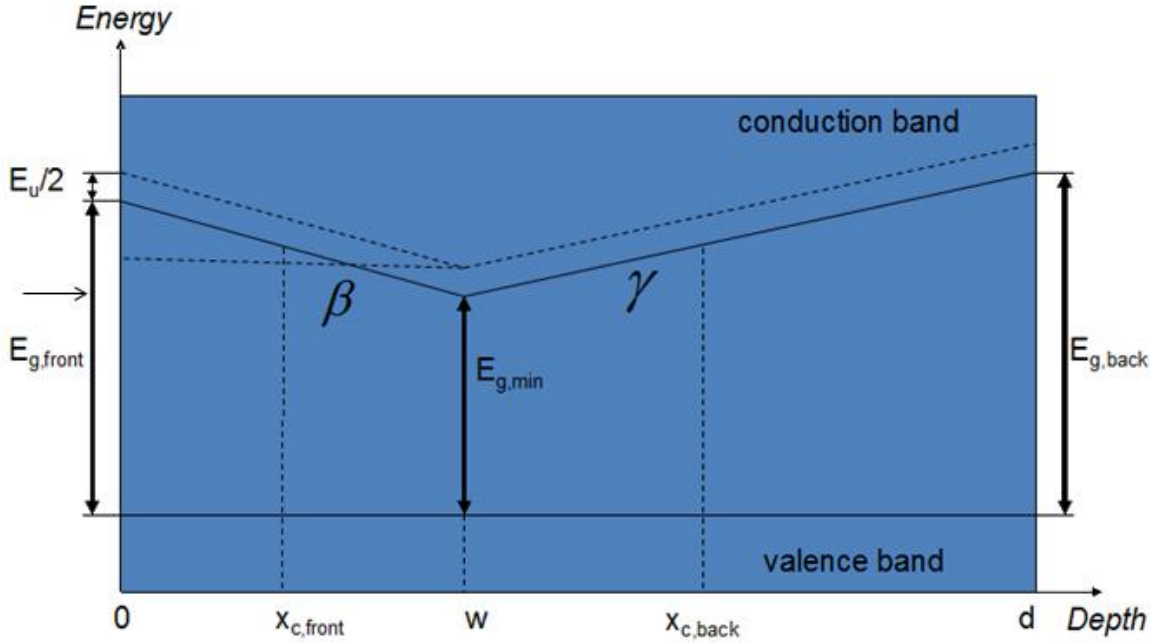


Figure 5.4 Energy diagram of a double-graded band gap absorber. Light is incident from the left.

The position-dependent band gap is given by:

$$E_g(0 \leq x \leq w) = E_{front} - \beta x = (w - x)\beta + E_{min} \quad (5.17)$$

$$E_g(w < x \leq d) = E_{min} + (x - w)\gamma = E_{back} - (d - x)\gamma \quad (5.18)$$

β and γ are grading parameters which are defined as follows:

$$\beta = \frac{E_{front} - E_{min}}{w} \quad (5.19)$$

$$\gamma = \frac{E_{back} - E_{min}}{(d - w)} \quad (5.20)$$

According to Eq. (5.13), a photon with energy between $E_{min}+E_U/2$ and $E_{front}+E_U/2$ will be absorbed through the Urbach tail from $x=0$ up to the coordinate x_{front} where band to band absorption begins. When $h\nu = E_{min}+E_U/2$, the layer thickness is w .

As in the previous analysis, a photon with energy between E_{min} and E_{back} will be absorbed by band to band absorption and sub-band gap absorption from $x=x_{back}$ to $x=d$. In order to proceed with the solution for Eq. (5.16), three absorption regimes are defined that yield different solutions for $\phi(x, h\nu)$:

Region 1: $h\nu < E_{min} + E_U / 2$, where only sub-band gap absorption takes place.

Region 2: $E_{min} + E_U / 2 \leq h\nu \leq E_{front} + E_U / 2$, where the range $x_{front} \leq x \leq x_{back}$ is band to band absorption; sub-band absorption takes place elsewhere.

Region 3: $h\nu > E_{front} + E_U / 2$, the range $x \leq x_{back}$ is band to band absorption; sub-band absorption takes place elsewhere.

5.6.3 Quantum Efficiency Calculations

The internal quantum efficiency (IQE) of solar cells, defined as the fraction of extracted charge carrier flux to absorbed photon flux, is critically determined by the absorption coefficient α of the material and the carrier collection function f_C of the cell. The internal quantum efficiency (IQE) of a photovoltaic absorber, between the depths x_1 and x_2 , is

defined by the integral:

$$IQE(h\nu) = \frac{\int_{x_2}^{x_1} G(x, h\nu) f_c(x) dx}{\phi_0(h\nu)} \quad (5.21)$$

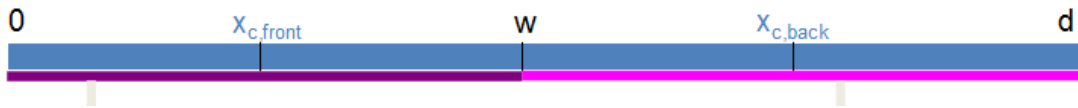
where, $G(x, h\nu)$ is the generation rate of carriers obtained and f_c is the probability that a carrier reaches the contact, contributing to the photocurrent [80].

The interpretation and analysis of experimental IQE curves depend strongly on the detailed knowledge of the absorption and electronic properties of the solar cell. Assume the case where carrier collection is perfect, i.e. $f_c=1$, and proceed to the non-ideal collection case. The IQE curves are obtained from [81]:

$$IQE_{\max}(h\nu) = \frac{\phi(x_1, h\nu) - \phi(x_2, h\nu)}{\phi(x_3, h\nu)} \quad (5.22)$$

The solution of photon flux ϕ of each region is shown below:

Solution in region 1:



When $0 \leq x \leq w$,

$$\phi(0 \leq x \leq w) = \phi_0 \exp \left\{ \frac{AE_U^{3/2}}{\sqrt{2}\beta} \exp \left(\frac{h\nu - E_U / 2 - E_{front}}{E_U} \right) \left[1 - \exp \left(\frac{\beta x}{E_U} \right) \right] \right\}$$

When $w < x \leq d$,

$$\phi(w < x \leq d) = \phi(w) \exp \left\{ \frac{AE_U^{3/2}}{\sqrt{2}\gamma} \exp \left(\frac{hv - E_U / 2 - E_{\min}}{E_U} \right) \left[\exp \left(\frac{(w-x)\gamma}{E_U} \right) - 1 \right] \right\}$$

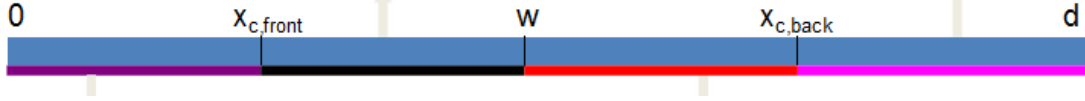
At $x = 0$, $\phi(0) = \phi_0$,

$$\text{At } x = w, \phi(w) = \phi_0 \exp \left\{ \frac{AE_U^{3/2}}{\sqrt{2}\beta} \exp \left(\frac{hv - E_U / 2 - E_{\text{front}}}{E_U} \right) \left[1 - \exp \left(\frac{E_{\text{front}} - E_{\min}}{E_U} \right) \right] \right\}$$

At $x = d$,

$$\phi(d) = \phi(w) \exp \left\{ \frac{AE_U^{3/2}}{\sqrt{2}\gamma} \exp \left(\frac{hv - E_U / 2 - E_{\text{back}}}{E_U} \right) - \frac{AE_U^{3/2}}{\sqrt{2}\gamma} \exp \left(\frac{hv - E_U / 2 - E_{\min}}{E_U} \right) \right\}$$

Solution in region 2:



When $0 \leq x \leq x_{\text{front}}$,

$$\phi(0 \leq x \leq x_{\text{front}}) = \phi_0 \exp \left\{ \frac{AE_U^{3/2}}{\sqrt{2}\beta} \exp \left(\frac{hv - E_U / 2 - E_{\text{front}}}{E_U} \right) \left[1 - \exp \left(\frac{\beta x}{E_U} \right) \right] \right\}$$

When $x_{\text{front}} \leq x \leq w$,

$$\phi(x_{\text{front}} < x \leq w) = \phi(x_{\text{front}}) \exp \left\{ \frac{2A}{3\beta} \left[\left(\frac{E_U}{2} \right)^{3/2} - (hv - E_{\text{front}} + \beta x)^{3/2} \right] \right\}$$

When $w \leq x \leq x_{\text{back}}$,

$$\phi(w < x \leq x_{\text{back}}) = \phi(w) \exp \left\{ \frac{2A}{3\gamma} [hv - E_{\text{back}} + (d-x)\gamma]^{3/2} - \frac{2A}{3\gamma} (hv - E_{\min})^{3/2} \right\}$$

When $x_{\text{back}} \leq x \leq d$,

$$\phi(x_{\text{back}} < x \leq d) = \phi(x_{\text{back}}) \exp \left\{ \frac{AE_U^{3/2}}{\sqrt{2}\gamma} \exp \left[\frac{hv - E_u / 2 + (d-x)\gamma}{E_U} \right] - \frac{AE_U^{3/2}}{\sqrt{2}\gamma} \right\}$$

At $x = 0$, $\phi(0) = \phi_0$

$$\text{At } x = x_{front}, \phi(x_{front}) = \phi_0 \exp \left\{ \frac{AE_U^{3/2}}{\sqrt{2}\beta} \exp \left(\frac{hv - E_U / 2 - E_{front}}{E_U} \right) - \frac{AE_U^{3/2}}{\sqrt{2}\beta} \right\}$$

$$\text{At } x = w, \phi(w) = \phi(x_{front}) \exp \left\{ \frac{2A}{3\beta} \left[\left(\frac{E_U}{2} \right)^{3/2} - (hv - E_{min})^{3/2} \right] \right\}$$

$$\text{At } x = x_{back}, \phi(x_{back}) = \phi(w) \exp \left\{ \frac{2A}{3\gamma} \left(\frac{E_U}{2} \right)^{3/2} - \frac{2A}{3\gamma} (hv - E_{min})^{3/2} \right\}$$

$$\text{At } x = d, \phi(d) = \phi(x_{back}) \exp \left\{ \frac{AE_U^{3/2}}{\sqrt{2}\gamma} \left[\exp \left(\frac{hv - E_U / 2 - E_{back}}{E_U} \right) - 1 \right] \right\}$$

Solution in region 3:



When $0 \leq x \leq w$,

$$\phi(0 \leq x \leq w) = \phi_0 \exp \left\{ \frac{2A}{3\beta} \left[(hv - E_{front})^{3/2} - (hv - E_{front} + \beta x)^{3/2} \right] \right\}$$

When $w \leq x \leq x_{back}$,

$$\phi(w < x \leq x_{back}) = \phi(w) \exp \left\{ \frac{2A}{3\gamma} [hv - E_{back} + (d - x)\gamma]^{3/2} - \frac{2A}{3\gamma} (hv - E_{min})^{3/2} \right\}$$

When $x_{back} \leq x \leq d$,

$$\phi(x_{back} < x \leq d) = \phi(x_{back}) \exp \left\{ \frac{AE_U^{3/2}}{\sqrt{2}\gamma} \exp \left[\frac{hv - E_U / 2 - E_{back} + (d - x)\gamma}{E_U} \right] - \frac{AE_U^{3/2}}{\sqrt{2}\gamma} \right\}$$

At $x = 0$, $\phi(0) = \phi_0$

$$\text{At } x = w, \phi(w) = \phi_0 \exp \left\{ \frac{2A}{3\beta} \left[(hv - E_{front})^{3/2} - (hv - E_{min})^{3/2} \right] \right\}$$

$$\text{At } x = x_{back}, \quad \phi(x_{back}) = \phi(w) \exp \left\{ \frac{2A}{3\gamma} \left[\left(\frac{E_U}{2} \right)^{3/2} - (hv - E_{min})^{3/2} \right] \right\}$$

$$\text{At } x = d, \quad \phi(d) = \phi(x_{back}) \exp \left\{ \frac{AE_U^{3/2}}{\sqrt{2}\gamma} \left[\exp \left(\frac{hv - E_U/2 - E_{back}}{E_U} \right) - 1 \right] \right\}$$

The quantum efficiency can be calculated according to Eq. (5.22) and the simulation result is shown in Figure 5.5 with the variation of β .

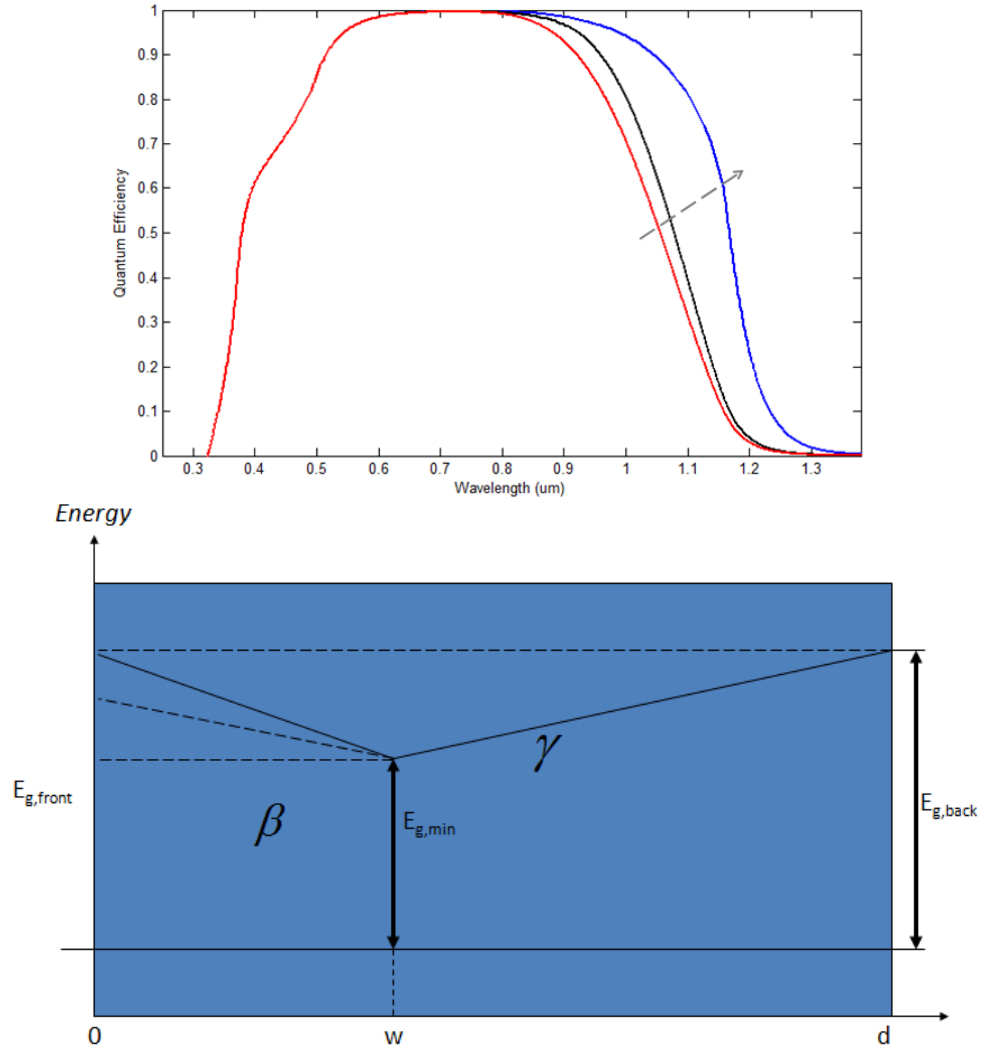


Figure 5.5 Internal quantum efficiency IQE vs. wavelength for various β . (Red $E_{front}=1.54$, $\beta=0.5$; purple $E_{front}=1.34$, $\beta=0.3$; blue $E_{front}=1.04$, $\beta=0$), assuming $A=5 \times 10^4 \text{ cm}^{-1} \text{ eV}^{-1/2}$, $E_{back}=1.54 \text{ eV}$, $E_{min}=1.04 \text{ eV}$, $w=1 \mu\text{m}$, $d=2 \mu\text{m}$, $E_U=0.03$.

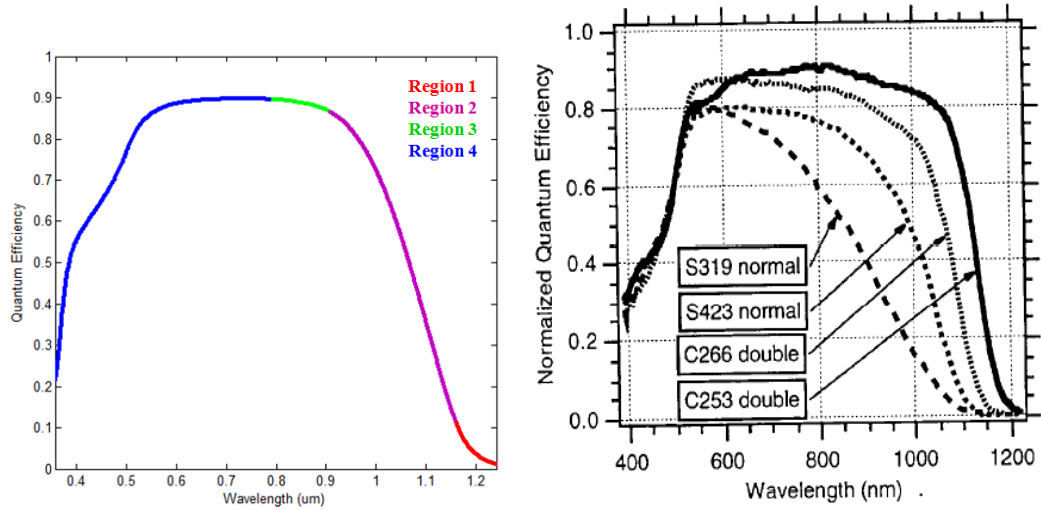


Figure 5.6 The comparison of simulation results and experimental results. Left is the simulation result which is internal quantum efficiency IQE vs. Wavelength. The red part is region 1, indigo part is region 2, green part is region 3 and blue part is region 4. On the right side is the experimental result: Normalized QE for selected devices incorporating absorbers with normal and double profiling. [82]

The diagram on the right side of Figure 5.6 shows the normalized quantum efficiency (QE) of selected normal and double profiling devices from Ref. [82]. The experimental data reveals that normal profiling devices do not collect efficiently in the long wavelengths. The double profiling devices, on the other hand, not only have an improved response in the long wavelengths but in the short wavelengths as well. Comparing the simulation results shown on the left with the experimental data, it fits well with the experimental results. As the gradient parameter β decreases, the quantum efficiency curve broadens in long wavelengths which is shown in Figure 5.6

5.6.4 Temperature-dependent Quantum Efficiency

The temperature dependence of the Urbach energy, E_U can be calculated from Eq. (5.11), assuming $A=0.15$, $B=0.025$ and the Debye temperature $\Theta=130\text{K}$. The temperature dependence of E_g is given by the Manoogian-Wolley relation, assuming $U=5\times 10^{-5}$, $V=3\times 10^{-4}$, $s=1$, $E_g(0)=1.04$.

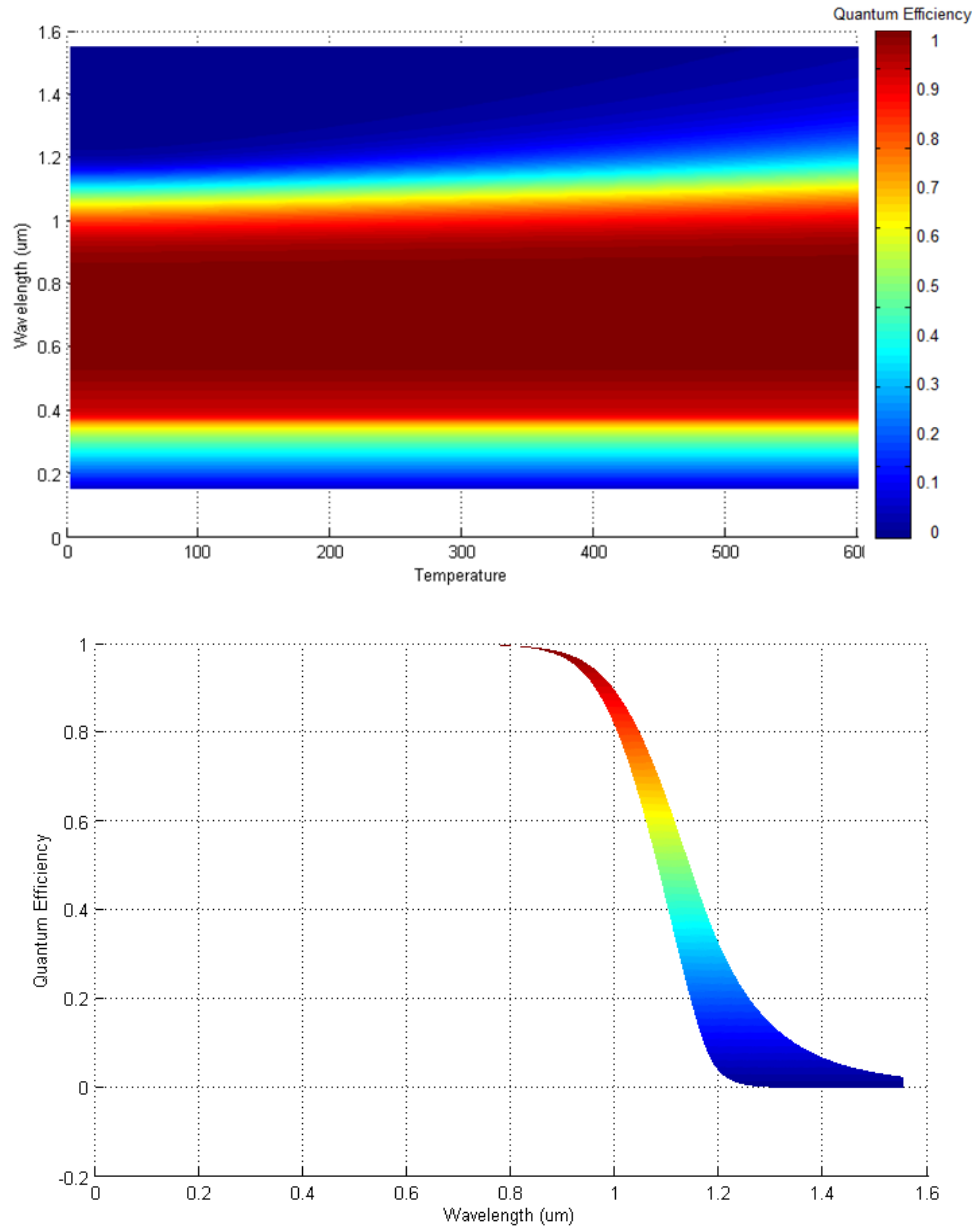


Figure 5.7 The quantum efficiency of the CIGS solar cell as a function of temperature and wavelength. The wavelength was varied from $0.2\mu\text{m}$ to $1.1\mu\text{m}$, and temperature from 0K to 600K .

The temperature dependence of the Urbach energy, E_U , can be calculated from Eq. (5.11), assuming $A=0.15$, $B=0.025$ and the Debye temperature $\Theta=130\text{K}$. The temperature dependence of E_g is calculated using the Manoogian-Wolley relation, assuming $U=5\times 10^{-5}$, $V=3\times 10^{-4}$, $s=1$, $E_g(0)=1.04$. The temperature dependence of quantum efficiency is shown in Figure 5.7. It indicates that, at short wavelengths, quantum efficiency does not vary with temperature. At long wavelengths, the quantum efficiency broadens with increasing temperature T .

CHAPTER 6

CONCLUSIONS

The physical phenomenon of quantum-mechanical tunneling is investigated especially in the non-parabolic band structure and with a variation of temperature. The conventional non-parabolic approximation of real band structures can be modified and generalized to approximate the complex band structures of common semiconductors with a significant improvement in accuracy in comparison with the parabolic approximation. The tunneling current density is calculated from a non-parabolic dispersion relation. In the calculations, the supply function is replaced by a step function and a series representation of the incomplete gamma function is used to reduce the solution. The tunneling current density is greatly influenced by the behavior of the band structure and the non-parabolic behavior of the band structure has additional contribution to the current density. Quantum-mechanical tunneling is investigated especially in the non-parabolic band structure and with a variation of temperature.

The quantum efficiency model based on CIGS solar cells has been discussed. In this model, the gradient parameters are discussed. The experimental data reveals that devices, with normal profile, do not collect efficiently in the long wavelengths. The double profile devices, on the other hand, not only have an improved response in the long wavelengths but in the short wavelengths as well. As the gradient parameter β increases, the quantum efficiency also increases in long wavelengths. The temperature-dependent quantum efficiency is investigated by modeling the temperature dependence of the Urbach energy and band gap based on CIGS solar cells. It indicates that, at short wavelengths, quantum efficiency does not vary with temperature. At long wavelengths, higher than $0.6\mu\text{m}$, the

quantum efficiency broadens with increasing temperature T .

APPENDIX

FERMI-DIRAC INTEGRALS

The selected Fermi-Dirac integrals are given in this appendix. Considering the integrals of the form,

$$I(p) = \int_0^{\infty} \frac{x^{p-1}}{e^x + 1} dx, \quad p > 1 \quad (\text{A.1})$$

We can solve them using the geometric series expansion:

$$\begin{aligned} I(p) &= \int_0^{\infty} \frac{x^{p-1}}{e^x + 1} dx = \int_0^{\infty} dx e^{-x} (1 + e^{-x})^{-1} x^{p-1} = \int_0^{\infty} dx e^{-x} \left[\sum_{k=0}^{\infty} (-1)^k (e^{-x})^k \right] x^{p-1} \quad (\text{A.2}) \\ &= \sum_{k=0}^{\infty} (-1)^k \int_0^{\infty} dx e^{-(k+1)x} x^{p-1} = \int_0^{\infty} dx e^{-x} x^{p-1} \Big|_{(k+1)x = y, dx = dy / (k+1)} \\ &= \sum_{k=0}^{\infty} (-1)^k \frac{1}{(k+1)^p} \int_0^{\infty} dy y^{p-1} e^{-y} \\ &= -\Gamma(p) \sum_{k=1}^{\infty} (-1)^k \frac{1}{k^p} \\ &= -\Gamma(p) \left(\sum_{k \text{ even}} \frac{1}{k^p} - \sum_{k \text{ odd}} \frac{1}{k^p} \right) = -\Gamma(p) \left(\frac{2}{2^p} \sum_{l=1}^{\infty} \frac{1}{l^p} - \sum_{k=1}^{\infty} \frac{1}{k^p} \right) \\ &= \left(1 - \frac{2}{2^{p-1}} \right) \zeta(p) \Gamma(p) \end{aligned}$$

where, $\zeta(p)$ is the Riemann *zeta* function, and $\Gamma(p)$ is the Euler *beta* function.

Selected Fermi-Dirac integrals are summarized in the following table:

Table A.1 Selected Fermi-Dirac Integrals

p	$\zeta(p)$	$\Gamma(p)$	$I = (1-1/2^{p-1})\zeta(p)\Gamma(p)$
3/2	2.612	$\sqrt{\pi}/2$	$0.383\sqrt{\pi}$
5/2	1.314	$3\sqrt{\pi}/4$	$0.650\sqrt{\pi}$
2	$\pi^2/6$	1	$\pi^2/12$
3	1.202	2	1.803
4	$\pi^4/90$	6	$7\pi^4/120$
6	$\pi^6/945$	120	$31\pi^6/252$

REFERENCES

- [1] Varshni, Y. P. (1967). Temperature dependence of the energy gap in semiconductors. *Physica*, 34(1), 149-154.
- [2] Nepal, N., Li, J., Nakarmi, M. L., Lin, J. Y., & Jiang, H. X. (2005). Temperature and compositional dependence of the energy band gap of AlGaIn alloys. *Applied Physics Letters*, 87(24), 242104-242104.
- [3] Pejova, B., Abay, B., & Bineva, I. (2010). Temperature dependence of the band-gap energy and sub-band-gap absorption tails in strongly quantized ZnSe nanocrystals deposited as thin films. *The Journal of Physical Chemistry C*, 114(36), 15280-15291.
- [4] Sarswat, P. K., & Free, M. L. (2012). A study of energy band gap versus temperature for Cu₂ZnSnS₄ thin films. *Physica B: Condensed Matter*, 407(1), 108-111.
- [5] Sze, S. M., & Ng, K. K. (2006). *Physics of semiconductor devices*. New York, NY: Wiley.
- [6] Fan, H. Y. (1951). Temperature dependence of the energy gap in semiconductors. *Physical Review*, 82(6), 900.
- [7] Odonnell, K. P., & Chen, X. (1991). Temperature dependence of semiconductor band gaps. *Applied Physics Letters*, 58(25), 2924-2926.
- [8] Grundmann, M. (2006). *The physics of semiconductors: an introduction including devices and nanophysics*. New York, NY: Springer.
- [9] Kane, E. O. (1957). Band structure of indium antimonide. *Journal of Physics and Chemistry of Solids*, 1(4), 249-261.
- [10] Nakwaski, W. (1995). Effective masses of electrons and heavy holes in GaAs, InAs, AlAs and their ternary compounds. *Physica B: Condensed Matter*, 210(1), 1-25.
- [11] Raymond, A., Robert, J. L., & Bernard, C. (1979). The electron effective mass in heavily doped GaAs. *Journal of Physics C: Solid State Physics*, 12(12), 2289.
- [12] Van Driel, H. M. (1984). Optical effective mass of high density carriers in silicon. *Applied Physics Letters*, 44(6), 617-619.
- [13] Cavassilas, N., Autran, J. L., Aniel, F., & Fishman, G. (2002). Energy and temperature dependence of electron effective masses in silicon. *Journal of Applied Physics*, 92(3), 1431-1433.

- [14] Riffe, D. M. (2002). Temperature dependence of silicon carrier effective masses with application to femtosecond reflectivity measurements. *JOSA B*, 19(5), 1092-1100.
- [15] Palik, E. D., Picus, G. S., Teitler, S., & Wallis, R. F. (1961). Infrared cyclotron resonance in InSb. *Physical Review*, 122(2), 475.
- [16] Hopkins, M. A., Nicholas, R. J., Brummell, M. A., Harris, J. J., & Foxon, C. T. (1987). Cyclotron-resonance study of nonparabolicity and screening in GaAsGa_{1-x}Al_xAs heterojunctions. *Physical Review B*, 36(9), 4789.
- [17] Hrivnak, L. (1992). Simple calculations of energy levels in quantum wells of lattice-matched semiconductors with nonparabolic bands. *Journal of Applied Physics*, 71(9), 4370-4376.
- [18] Hrivnak, L. (1990). Determination of Γ electron and light hole effective masses in Al_xGa_{1-x}As on the basis of energy gaps, band-gap offsets, and energy levels in Al_xGa_{1-x}As/GaAs quantum wells. *Applied Physics Letters*, 56(24), 2425-2427.
- [19] Chamberlain, J. M., Simmonds, P. E., Stradling, R. A., & Bradley, C. C. (1971). Cyclotron resonance with epitaxial films of n type inp. *Journal of Physics C: Solid State Physics*, 4(2), L38.
- [20] Zener, C. (1934). A theory of the electrical breakdown of solid dielectrics. *Proceedings of the Royal Society of London. Series A, Containing Papers of a Mathematical and Physical Character*, 145(855), 523-529.
- [21] Klingshirn, C. F. (2012). *Semiconductor optics*. New York, NY: Springer.
- [22] Aydin, C., Zaslavsky, A., Luryi, S., Cristoloveanu, S., Mariolle, D., Fraboulet, D., & Deleonibus, S. (2004). Lateral interband tunneling transistor in silicon-on-insulator. *Applied Physics Letters*, 84(10), 1780-1782.
- [23] Appenzeller, J., Lin, Y. M., Knoch, J., & Avouris, P. (2004). Band-to-band tunneling in carbon nanotube field-effect transistors. *Physical Review Letters*, 93(19), 196805.
- [24] Bhuwalka, K. K., Schulze, J., & Eisele, I. (2005). Scaling the vertical tunnel FET with tunnel bandgap modulation and gate workfunction engineering. *Electron Devices, IEEE Transactions on*, 52(5), 909-917.
- [25] Nayfeh, O. M., Chleirigh, C. N., Hennessy, J., Gomez, L., Hoyt, J. L., & Antoniadis, D. A. (2008). Design of tunneling field-effect transistors using strained-silicon/strained-germanium type-II staggered heterojunctions. *Electron Device Letters, IEEE*, 29(9), 1074-1077.

- [26] Verhulst, A. S., Vandenberghe, W. G., Maex, K., De Gendt, S., Heyns, M. M., & Groeseneken, G. (2008). Complementary silicon-based heterostructure tunnel-FETs with high tunnel rates. *Electron Device Letters, IEEE*, 29(12), 1398-1401.
- [27] Kane, E. O. (1960). Zener tunneling in semiconductors. *Journal of Physics and Chemistry of Solids*, 12(2), 181-188.
- [28] Kane, E. O. (1961). Theory of tunneling. *Journal of Applied Physics*, 32(1), 83-91.
- [29] Kane, E. O., & Blount, E. I. (1969). *Tunneling phenomena in solids*. New York, NY: Springer.
- [30] Maserjian, J. (1974). Tunneling in thin MOS structures. *Journal of Vacuum Science and Technology*, 11(6), 996-1003.
- [31] Register, L. F., Rosenbaum, E., & Yang, K. (1999). Analytic model for direct tunneling current in polycrystalline silicon-gate metal-oxide-semiconductor devices. *Applied Physics Letters*, 74(3), 457-459.
- [32] Bjork, M. T., Knoch, J., Schmid, H., Riel, H., & Riess, W. (2008). Silicon nanowire tunneling field-effect transistors. *Applied Physics Letters*, 92(19), 193504-193504.
- [33] Boucart, K., & Ionescu, A. M. (2007). Double-gate tunnel FET with high- κ gate dielectric. *Electron Devices, IEEE Transactions on*, 54(7), 1725-1733.
- [34] Banerjee, S. A. N. J. A. Y., Richardson, W., Coleman, J., & Chatterjee, A. M. I. T. A. V. A. (1987). A new three-terminal tunnel device. *Electron Device Letters, IEEE*, 8(8), 347-349.
- [35] Fair, R. B., & Wivell, H. W. (1976). Zener and avalanche breakdown in As-implanted low-voltage Si np junctions. *Electron Devices, IEEE Transactions on*, 23(5), 512-518.
- [36] Zhang, Q., Zhao, W., & Seabaugh, A. (2006). Low-subthreshold-swing tunnel transistors. *Electron Device Letters, IEEE*, 27(4), 297-300.
- [37] Jiménez, D., Cartoixa, X., Miranda, E., Suñé, J., Chaves, F. A., & Roche, S. (2006). A drain current model for Schottky-barrier CNT-FETs. *Journal of Computational Electronics*, 5(4), 361-364.
- [38] Guan, X., Kim, D., Saraswat, K. C., & Wong, H. S. (2011). Complex band structures: from parabolic to elliptic approximation. *Electron Device Letters, IEEE*, 32(9), 1296-1298.
- [39] Gehring, A., & Selberherr, S. (2004). Modeling of tunneling current and gate dielectric reliability for nonvolatile memory devices. *Device and Materials Reliability, IEEE Transactions on*, 4(3), 306-319.

- [40] Jeon, K. (2012). *Band-to-Band Tunnel Transistor Design and Modeling for Low Power Applications*. CALIFORNIA UNIV BERKELEY DEPT OF ELECTRICAL ENGINEERING AND COMPUTER SCIENCE.
- [41] Majumdar, A., Lauer, I., & O'Regan, T. (2010). Universality of Zener tunneling in homojunction pn diodes. *Journal of Applied Physics*, 108(2), 024501-024501.
- [42] Flietner, H. (1972). The $E(k)$ relation for a two-band scheme of semiconductors and the application to the metal-semiconductor contact. *Physica Status Solidi (b)*, 54(1), 201-208.
- [43] Gasiorowicz, S. (2007). *Quantum physics*. New York, NY: Wiley.
- [44] Altschul, V. A., Fraenkel, A., & Finkman, E. (1992). Effects of band nonparabolicity on two-dimensional electron gas. *Journal of Applied Physics*, 71(9), 4382-4384.
- [45] Bandara, K. M. S. V., & Coon, D. D. (1989). Derivation and correction of the Tsu-Esaki tunneling current formula. *Journal of Applied Physics*, 66(2), 693-696.
- [46] Van Halen, P., & Pulfrey, D. L. (1985). Accurate, short series approximations to Fermi-Dirac integrals of order-1/2, 1/2, 1, 3/2, 2, 5/2, 3, and 7/2. *Journal of Applied Physics*, 57(12), 5271-5274.
- [47] Penley, J. C. (1962). Tunneling through thin films with traps. *Physical Review*, 128(2), 596.
- [48] Rieth, M., & Schommers, W. (2006). *Handbook of theoretical and computational nanotechnology*. Stevenson Ranch, CA: American Scientific Publishers.
- [49] Abramowitz, M., & Stegun, I. A. (1964). *Handbook of mathematical functions: with formulas, graphs, and mathematical tables*. New York, NY: Dover Publications.
- [50] Amore, P. (2005). Asymptotic and exact series representations for the incomplete Gamma function. *EPL (Europhysics Letters)*, 71(1), 1.
- [51] Aydin, C., Zaslavsky, A., Luryi, S., Cristoloveanu, S., Mariolle, D., Fraboulet, D., & Deleonibus, S. (2004). Lateral interband tunneling transistor in silicon-on-insulator. *Applied Physics Letters*, 84(10), 1780-1782.
- [52] Luque, A., & Hegedus, S. (2011). *Handbook of photovoltaic science and engineering*. New York, NY: Wiley.
- [53] Lundberg, O., Edoff, M., & Stolt, L. (2005). The effect of Ga-grading in CIGS thin film solar cells. *Thin Solid Films*, 480, 520-525.
- [54] Palm, J., Probst, V., & Karg, F. H. (2004). Second generation CIS solar modules. *Solar Energy*, 77(6), 757-765.

- [55] Gabor, A. M., Tuttle, J. R., Bode, M. H., Franz, A., Tennant, A. L., Contreras, M. A., & Hermann, A. M. (1996). Band-gap engineering in Cu (In, Ga) Se₂ thin films grown from (In, Ga)₂Se₃ precursors. *Solar Energy Materials and Solar Cells*, 41, 247-260.
- [56] Gloeckler, M. (2005). *Device physics of Cu(In, Ga)Se₂ thin-film solar cells* (Doctoral dissertation, Colorado State University).
- [57] Smole, F., & Furlan, J. (1996). Band-gap engineering in CdS/Cu (In, Ga)Se₂ solar cells. *Journal of Applied Physics*, 79(11), 8537-8540.
- [58] Troviano, M., & Taretto, K. (2011). Analysis of internal quantum efficiency in double-graded bandgap solar cells including sub-bandgap absorption. *Solar Energy Materials and Solar Cells*, 95(3), 821-828.
- [59] Kniese, R., Hariskos, D., Voorwinden, G., Rau, U., & Powalla, M. (2003). High band gap Cu (In, Ga)Se₂ solar cells and modules prepared with in-line co-evaporation. *Thin Solid Films*, 431, 543-547.
- [60] Gloeckler, M., & Sites, J. R. (2005). Band-gap grading in Cu(In, Ga)Se₂ solar cells. *Journal of Physics and Chemistry of Solids*, 66(11), 1891-1894.
- [61] Gabor, A. M., Tuttle, J. R., Bode, M. H., Franz, A., Tennant, A. L., Contreras, M. A., & Hermann, A. M. (1996). Band-gap engineering in Cu (In, Ga) Se₂ thin films grown from (In, Ga)₂Se₃ precursors. *Solar Energy Materials and Solar Cells*, 41, 247-260.
- [62] Jackson, P., Hariskos, D., Lotter, E., Paetel, S., Wuerz, R., Menner, R., & Powalla, M. (2011). New world record efficiency for Cu(In, Ga)Se₂ thin-film solar cells beyond 20%. *Progress in Photovoltaics: Research and Applications*, 19(7), 894-897.
- [63] Dasgupta, P. K., Eom, I. Y., Morris, K. J., & Li, J. (2003). Light emitting diode-based detectors: Absorbance, fluorescence and spectroelectrochemical measurements in a planar flow-through cell. *Analytica Chimica Acta*, 500(1), 337-364.
- [64] Schubert, E. F., Gessmann, T., & Kim, J. K. (2005). *Light emitting diodes*. New York, NY: John Wiley & Sons, Inc..
- [65] Dow, J. D., & Redfield, D. (1972). Toward a unified theory of Urbach's rule and exponential absorption edges. *Physical Review B*, 5(2), 594..
- [66] Grein, C. H., & John, S. (1989). Temperature dependence of the Urbach optical absorption edge: A theory of multiple phonon absorption and emission sidebands. *Physical Review B*, 39(2), 1140.

- [67] Studenyak, I. P., Kranjčec, M., & Koperlyos, B. M. (2009). On the Urbach rule in SbSI ferroelectric crystal. *Ukr. J. Phys. Opt.*, *10*(2), 61.
- [68] Kunets, V. P., Kulish, N. R., Kunets, V. P., & Lisitsa, M. P. (2002). Urbach's rule peculiarities in structures with $\text{CdS}_x\text{Se}_{1-x}$ nanocrystals. *Semiconductor Physics, Quantum Electronics & Optoelectronics*, *5*(1): 9-15.
- [69] Cody, G. D., Tiedje, T., Abeles, B., Brooks, B., & Goldstein, Y. (1981). Disorder and the optical-absorption edge of hydrogenated amorphous silicon. *Physical Review Letters*, *47*(20), 1480.
- [70] Wasim, S. M., Rincon, C., & Sanchez Perez, G. (1998). Urbach–Martienssen's tail in the absorption spectra of the ordered vacancy compound CuIn_3Se_5 . *Journal of Applied Physics*, *84*(10), 5823-5825.
- [71] Rakhshani, A. E. (2000). Study of Urbach tail, bandgap energy and grain-boundary characteristics in CdS by modulated photocurrent spectroscopy. *Journal of Physics: Condensed Matter*, *12*(19), 4391.
- [72] Manoogian, A., & Woolley, J. C. (1984). Temperature dependence of the energy gap in semiconductors. *Canadian Journal of Physics*, *62*(3), 285-287.
- [73] Fonthal, G., Tirado-Mejia, L., Marin-Hurtado, J. I., Ariza-Calderon, H., & Mendoza-Alvarez, J. G. (2000). Temperature dependence of the band gap energy of crystalline CdTe. *Journal of Physics and Chemistry of Solids*, *61*(4), 579-583.
- [74] Rivero, A., Quintero, M., Power, C., Gonzalez, J., Tovar, R., & Ruiz, J. (1997). Temperature variation of optical energy gap values of the compound CuGaTe_2 . *Journal of Electronic Materials*, *26*(12), 1428-1432.
- [75] Lárez, C., Bellabarba, C., & Rincón, C. (1994). Alloy composition and temperature dependence of the fundamental absorption edge in $\text{CuGa}_x\text{In}_{1-x}\text{Se}_2$. *Applied Physics Letters*, *65*(13), 1650-1652.
- [76] Mattheis, J., Rau, U., & Werner, J. H. (2007). Light absorption and emission in semiconductors with band gap fluctuations—A study on $\text{Cu}(\text{In}, \text{Ga})\text{Se}_2$ thin films. *Journal of Applied Physics*, *101*(11), 113519-113519.
- [77] Kirchartz, T., Rau, U., Kurth, M., Mattheis, J., & Werner, J. H. (2007). Comparative study of electroluminescence from $\text{Cu}(\text{In}, \text{Ga})\text{Se}_2$ and Si solar cells. *Thin Solid Films*, *515*(15), 6238-6242.
- [78] Kirchartz, T., & Rau, U. (2007). Electroluminescence analysis of high efficiency CuInGaSe_2 solar cells. *Journal of Applied Physics*, *102*(10), 104510-104510.
- [79] Grove, A. S. (1967). *Physics and technology of semiconductor devices*. New York, NY: Wiley.

- [80] Green, M. A. (2009). Do built-in fields improve solar cell performance?. *Progress in Photovoltaics: Research and Applications*, 17(1), 57-66.
- [81] Chuang, S. L. (2012). *Physics of photonic devices*. New York, NY: John Wiley & Sons.
- [82] Contreras, M. A., Tuttle, J., Gabor, A., Tennant, A., Ramanathan, K., Asher, S., & Noufi, R. (1994). High efficiency Cu (In, Ga) Se₂-based solar cells: processing of novel absorber structures. In *Photovoltaic Energy Conversion, 1994., Conference Record of the Twenty Fourth. IEEE Photovoltaic Specialists Conference-1994, 1994 IEEE First World Conference on* (Vol. 1, pp. 68-75). IEEE.
- [83] Poortmans, J., & Arkhipov, V. (2006). *Thin film solar cells: fabrication, characterization and applications*. New York, NY: John Wiley & Sons.
- [84] Ravindra, N. M., Auluck, S., & Srivastava, V. K. (1979). Temperature dependence of the energy gap in PbS, PbSe, and PbTe. *Physica Status Solidi (a)*, 52(2), K151-K155.